# Ultra-peripheral J/$\psi$ production in PbPb collisions at $\sqrt{s_{NN}}$=2.76 TeV with CMS

By

## R. Patrick Kenny III

Submitted to the Department of People who read Abstracts and the
Graduate Faculty of the University of Kansas
in partial fulfillment of the requirements for the degree of
Doctor of Philosophy

Committee members

| | |
|---|---|
| MEMBER 1, Chairperson | |
| MEMBER 2 | |
| MEMBER 3 | |
| MEMBER 4 | |

Date defended: _____ October 02, 2012

The Dissertation Committee for R. Patrick Kenny III certifies
that this is the approved version of the following dissertation :

Ultra-peripheral J/$\psi$ production in PbPb collisions at $\sqrt{s_{NN}}$=2.76 TeV with CMS

_____

MEMBER 1, Chairperson

Date approved: _____ October 03, 2012 _____

# Abstract

The first is some LaTeX code, don't change it.

# Acknowledgements

I would like to thank all of the little people who made this thesis possible.

# Contents

# List of Figures

ix

# List of Tables

# Chapter 1

# Introduction

## 1.1   Theoretical Context

## 1.2   History

# Chapter 2

# Theory

## 2.1 Introduction

Microseconds after the big bang, the universe existed in a state known as the Quark Gluon Plasma (QGP). In the QGP, quarks and gluons are not in hadronic bondage, forced to the confines of bound states such as protons and neutrons. The Large Hadron Collider (LHC) produces QGP in the lab in PbPb (lead-lead) collisions. The high energies and rates of the collisions at the LHC make it possible to do detailed studies of the QGP. The LHC is producing rare experimental probes such as suppressed jets and heavy quarkonia at an unprecedented rate in heavy-ion collisions. Physicists now have better constraints on the properties like temperature, viscosity, and energy density of the QGP.

The detailed studies of PbPb collisions coming out of the LHC experiments require an understanding of the initial state of the ions before they collide. Without knowledge of the initial state, physicists cannot determine which experimental effects are due to the QGP and which effects are inherent to the nuclei themselves. For example, suppression of heavy quarkonia is a signature of the QGP but also appears to occur in deuterium-gold collisions where the QGP is not expected to arise [3]. Because it is not certain how much of the reduction of quarkonia production is due to the initial state of the nuclei, the reduction due to the QGP is unclear. Without a clean probe of the

initial state, physicists' knowledge of the QGP is limited. Ultra-Peripheral Collisions (UPC) at the LHC fill this need for a clean probe.

The colliding nuclei interact electromagnetically in an UPC event, avoiding the complicated mixing of final state and initial state effects found in nuclear collisions. In UPC events, no QGP state emerges, and the effects arising from the QGP no longer obscure the initial state effects. Other initial state probes such as peripheral nuclear collisions and proton-nucleus collisions have the potential to create the QGP obscuring which effects come from the initial state. It is impossible to create the QGP in UPC events because the nucleons within the nucleus do not collide. UPC events provide clarity by enhancing physicists' understanding of the initial state.

The interactions between the field of photons surrounding the colliding nuclei and the gluons of nuclei can produce a $J/\psi$ probing the gluon density. The UPC $J/\psi$ photoproduction cross section is therefore a probe of the initial state of the nucleus. The Weizsiäcker-Williams approximation provides a way to calculate the density of probing photons that surrounds the nucleus. The electron-proton scattering data gives a value for the proton photoproduction cross section at lower energies. The perterbutive Quantum Chromo-dynamics (pQCD), Vector Messon Dominance (VMD), and Leading Twist (LTA) methods all combined the nuclear photon flux with the proton scattering data to calculate the nuclear photoproduction cross section. Each of these methods handle the gluon density of the nucleus differently producing a measurable difference in the value of the $J/\psi$ photoproduction cross section.

## 2.2 QCD/QGP

## 2.3 CGC/intial state

The color glass condensate (CGC) is an effective theory of parton saturation and coupling that aims to explain the initial state of hadronic matter in high energy heavy ions collisions [4]. CGC was developed to calculate the distribution of partons within a nucleus. The theory's name is instructive

of how this is achieved [1]. The first term color steams simply from the fact that the partons carry a color charge. The second terms refers to a coupling within the theory of the low momentum partons to the high momentum partons. In CGC the low momentum partons take on the time scales of the higher momentum partons, which can be described perturbatively. This behavior is analogous to glass, which behaves like a solid on short time scales and a liquid on long time scales. The last term condensate refers to saturation. The CGC predicts that as the hadronic matter is boosted to higher and higher energies, low momentum states are filled and become increasingly less favorable to higher momentum states. In the theory the higher momentum states are treated as the source of the lower momentum states in the same manor that an electron is the source of an electric and magnetic field. This couples the low momentum partons to the weakly coupled high momentum partons.
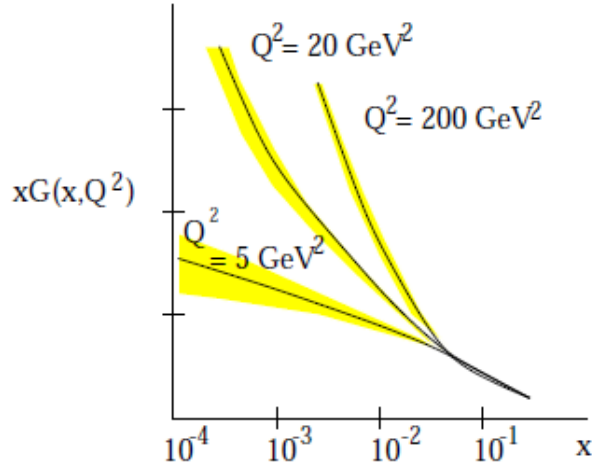


Figure 2.1: A representation of HERA deep inelastic scattering data, which shows the accumulation of low-x partons from Reference [1].

The CGC was inspired by and gives a natural explanation of deep inelastic scattering data. Figure 2.1 gives a representation of the data collected by the HERA experiment. The HERA data shows that as the constituents of a heavy ion are explored the number constituents at lower momentum grows. Following from right to left in Figure 2.1 the gluon density increases as $x$ decreases, where $x$ is the fraction of the total momentum the constituent holds. The number of low momentum constituents can not however grow with out bound, a plateau must emerge. A

plateau is required in order to assure unitarity, which requires that the probability of scattering off the nucleus does not exceed one. Emergence of a plateau would indicate evidence of saturation, the point where it becomes less favorable to produce more low momentum constituents. As seen in Figure 2.1, the saturation scale increases as the momentum transfered to the probe $Q^2$ increases. This effect suggests that the saturation scale can be used to measure the running of the strong coupling constant predicted by standard perturbative QCD.

## 2.4  Weizsäcker-Williams Approximation

The Weizsiäcker-Williams approximation relates the electric field of a stationary point charge to the photon field that arises at ultra relativistic velocities. The approximation is semi-classical and combines both classical and quantum elements. A Fourier transform of Maxwell's equations combine with Einstein's equation for the energy of a photon in the Weizsiäcker-Williams approximation. The frequency modes of the electrostatic field are treated as photons. The conversion of the electric field to a flux of photons simplifies the calculation of interaction cross sections. The Weizsiäcker-Williams approximation makes the



Figure 2.2:  The electromagnetic field boosted and at rest.

calculation of electromagnetic interactions with the nucleus tractable.

The Wiezacker-Williams approximation begins with the equation for the electric field of the projectile nucleus at rest. The electromagnetic field only needs to be considered at the position of

the target nucleus. From the projectile's point of view, the target is moving and contributes $-vt$ to Eq. 2.1, the equation for the electric field of the projectile nucleus at rest.

$$x' = -vt' \qquad y' = b \qquad z' = 0 \qquad \vec{\mathbf{E}}' = \left( \frac{eZ}{4\pi\varepsilon_0 \left( (-vt')^2 + b^2 \right)^{3/2}} \right) \left( -vt'\hat{\mathbf{x}}' + b\hat{\mathbf{y}}' \right) \qquad (2.1)$$

In Eq. 2.1, $b$ is the impact parameter, the distance of separation at closest approach, $v$ is the velocity of the projectile nucleus, $Z$ is the number of protons in the nucleus, and $e$ is the charge of the electron. Two simplifications occur due to the coordinates of Eq. 2.1. The magnetic field is equal to zero, because the projectile is at rest, and the $z$ coordinate can be ignored, reducing the equation to two dimensions.

The Lorentz transformation converts the field equations in the projectile's frame to equations in the target's frame. The result is a set of equations that relate the electric and magnetic field components in one frame to the components of the electric and magnetic field in another frame moving at a different constant velocity. Eq. 2.2 gives the result of the transformation from the projectile's primed frame to the target's rest frame for the field components [5]:

$$E'_x = E_x \qquad \gamma \left( E'_y/c + \beta B'_z \right) = E_y/c \qquad \gamma \left( E'_z/c = \beta B'_y \right) = E_z/c$$

$$B'_x = B_x \qquad \gamma \left( B'_y - \beta E'_z/c \right) = B_y \qquad \gamma \left( B'_z + \beta E'_y/c \right) = B_z \qquad (2.2)$$

The transformation equations for the fields, Eq. 2.2, and the transformation of the coordinates reduce to Eq. 2.3 [5]:

$$E'_x = E_x \qquad \gamma E'_y = E_y \qquad \gamma \beta E'_y/c = B_z$$

$$ct' = \gamma ct \qquad x' = -\gamma \beta ct \qquad (2.3)$$

The simplicity of Eq. 2.1 creates the simplicity of Eq. 2.2. The Lorentz transformation reduces the six components of the electromagnetic field in the target's frame to the three equations in Eq. 2.2

by relating them to the fields of the projectile's frame.

The combination of Eq. 2.1 and Eq. 2.2 produce equations for the electric and magnetic fields in the target's rest frame. Eq. 2.1 gives the expression for the field components as seen in the projectile frame.

$$\vec{\mathbf{E}} = \left( \frac{\gamma e Z}{4\pi\varepsilon_0 \left( (\gamma v t)^2 + b^2 \right)^{3/2}} \right) (vt\hat{\mathbf{x}} + b\hat{\mathbf{y}})$$

$$\vec{\mathbf{B}} = \frac{\gamma \beta e Z b}{4\pi c\varepsilon_0 \left( (\gamma v t)^2 + b^2 \right)^{3/2}}\hat{\mathbf{z}} = \frac{\gamma \mu_0 v e Z b}{4\pi \left( (\gamma v t)^2 + b^2 \right)^{3/2}}\hat{\mathbf{z}} \qquad (2.4)$$

If the impact parameter $b$ goes to zero, the target sits in the line of the projectile particle's motion, and the denominator carries a factor of $\gamma$ squared. If $vt$ goes to zero, the projectile particle is directly above or below in the $y$ direction, and the numerator carries a factor of $\gamma$. This results in fields that are a factor of $\gamma^3$ higher in the $y$ direction than in the $x$ direction (see Fig. 2.2). The boost compresses the electric field of the charge in the direction of the boost and produces a magnetic field resulting in a form similar to radiation. The point charge at ultra relativistic velocities produces a strong electric field in the plane transverse to its motion resembling a plane wave.

Separating the even and odd functions of the electromagnetic field simplify the decomposition of the field equations into Fourier modes. The even functions decompose into cosine functions, odd functions into sine functions. The y-component of the electric field and the z-component of the magnetic field are even functions in time, and the x-component of the electric field is an odd function in time. Eq. 2.5 gives the Fourier transformation integrals.

$$E_x(\omega) = \sqrt{\frac{2}{\pi}}\frac{eZ}{4\pi\varepsilon_0 b^2}\int_0^{\infty}\frac{(\gamma v t/b)\sin(\omega t)}{\left( (\gamma v t/b)^2 + 1 \right)^{3/2}}dt \qquad E_y(\omega) = \sqrt{\frac{2}{\pi}}\frac{\gamma eZ}{4\pi\varepsilon_0 b^2}\int_0^{\infty}\frac{\cos(\omega t)}{\left( (\gamma v t/b)^2 + 1 \right)^{3/2}}dt$$

$$B_z(\omega) = \frac{\beta E_y(\omega)}{c} \qquad (2.5)$$

With the appropriate substitutions, tables provide solutions to the integrals of Eq. 2.5 as seen in Ref. [6].

$$u = \frac{\gamma vt}{b} \qquad du\left(\frac{b}{\gamma v}\right) = dt \qquad \omega' = \frac{\omega b}{\gamma v}$$

$$\int_0^\infty \frac{u\sin(\omega'u)}{(u^2+1)^{3/2}}du = \omega'K_0(\omega') \qquad \int_0^\infty \frac{\cos(\omega'u)}{(u^2+1)^{3/2}} = \omega'K_1(\omega') \qquad (2.6)$$

The Fourier transformation replaces the time variable with a frequency variable in the field equations. The frequency relates to photon energy by the Einstein's photon energy equation, $E = \hbar\omega$. The substitution of time with frequency allows for a flux of photons to replace the classical electromagnetic field.

The $\gamma$ dependence of the field components is different because of the different $t$ dependence of Eq. 2.6. The integrals in Eq. 2.6 shift the $\gamma$ dependence of the field component equations. Eq. 2.7 gives the result of the integrals:

$$E_x(\omega) = \sqrt{\frac{2}{\pi}}\frac{eZ}{4\pi\varepsilon_0 b^2}\frac{b}{\gamma v}\frac{\omega b}{\gamma v}K_0\left(\frac{\omega b}{\gamma v}\right) \qquad E_y(\omega) = \sqrt{\frac{2}{\pi}}\frac{\gamma eZ}{4\pi\varepsilon_0 b^2}\frac{b}{\gamma v}\frac{\omega b}{\gamma v}K_1\left(\frac{\omega b}{\gamma v}\right) \qquad (2.7)$$

$\gamma$ is subsumed into the substitution from $t$ to $\omega$ in the numerator of the x-component and becomes a part of the zeroth-order modified Bessel function upon integration. The y-component does not have a factor of $t$ in the numerator, therefore the factor of $\gamma$ remains outside of the integral, and it does not get subsumed into the first-order modified Bessel function. In Eq. 2.7, $E_y$ carries an additional factor of $\gamma$ in the numerator relative to the $E_x$. $E_y$ is $\gamma$ times larger then $E_x$.

In the ultra-relativistic limit, the electric and magnetic fields have the same configuration as electromagnetic plane wave radiation. The electric and magnetic fields are perpendic-
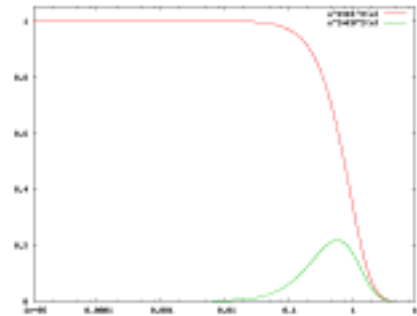


Figure 2.3: The zero and first order modified Bessel functions.

8

ular and related by a factor of $c$ in the ultra rel-

ativistic limit. When $v$ approaches $c$, $\beta \approx 1$,

the y-component of the electric field and the z-

component of the magnetic field are related by a factor of $c$, $E_y/c = B_z$. Because $K_0(x)$ is smaller

than $K_1(x)$ for all x, when $\gamma \gg 1$, $E_y$ is approximately equally to $\gamma E_x$. The conditions imposed

by the ultra-relativistic limit result in the relationship of Eq. 2.8.

$$\gamma \gg 1 \rightarrow \gamma E_x \gg E_x \rightarrow E_y \gg E_x \tag{2.8}$$

The x-component of the electric field can therefore be ignored and the magnetic and electric fields

are left perpendicular to each other. The six field components reduced to one electric component

and one perpendicular magnetic field component, which have a configuration identical to a plane

wave.

As with plane waves, the energy per area per time transfered by the electromagnetic field

is given by the Poynting vector. The Poynting vector takes the simple form of a plane pulse

propagating in the x direction.

$$\vec{S} \equiv \vec{E} \times \vec{B}/\mu_0 = \left(E_y^2/c\mu_0\right)\hat{\mathbf{x}} = c\varepsilon_0 E_y^2 \hat{\mathbf{x}} \tag{2.9}$$

The Poynting vector relates to the fluence (energy per unit area) [7],

$$I(b) = \hat{\mathbf{x}} \cdot \int_0^\infty \vec{S}d\omega = \int_0^\infty \left(c\varepsilon_0 E_y^2\right)d\omega = \int_0^\infty \left(\frac{dI}{d\omega}\right)d\omega \tag{2.10}$$

and the spectral fluence (energy per area per frequency).

$$\frac{dI}{d\omega} = c\varepsilon_0 E_y^2 = \frac{e^2 Z^2 c}{4\pi^3 b^2 v^2 \varepsilon_0}\left(\frac{\omega b}{\gamma v}\right)^2 K_1^2\left(\frac{\omega b}{\gamma v}\right) = \alpha\hbar\left(\frac{Z}{b\beta\pi}\right)^2\left(\frac{\omega b}{\gamma v}\right)^2 K_1^2\left(\frac{\omega b}{\gamma v}\right) \tag{2.11}$$

Substituting Eq. 2.7 into Eq. 2.10 gives the Poynting vector as a function of frequency. Eq. 2.11

9

paves the way for Einstein's equation. The spectral fluence given by Eq. 2.11 relates the frequency to energy, which are the same quantities present in Einstein's equation.

Einstein's equation, $E = \hbar\omega$, gives the energy of a photon, which is related to the spectral fluence. If the fluence is due to a photon number density, $N$, Einstein's equation relates $N$ to the fluence. The relationship between the number of photons per unit area in an infinitesimal energy range and the spectral fluence in an infinitesimal frequency range is given by Eq. 2.12 [5].

$$\frac{dI}{d\omega}d\omega = \hbar\omega N(\omega)d(\hbar\omega) \rightarrow \frac{1}{\hbar^2\omega}\frac{dI}{d\omega} = N(\omega) \tag{2.12}$$

Plugging Eq. 2.11 into Eq. 2.12 yields the semiclassical photon flux of an ultra-relativistic nucleus.

$$N(\omega,b) = \frac{\alpha}{\hbar\omega}\left(\frac{Z}{b\beta\pi}\right)^2\left(\frac{\omega b}{\gamma v}\right)^2 K_1^2\left(\frac{\omega b}{\gamma v}\right) \tag{2.13}$$

Eq. 2.13 replaces the classical electric field of a point charge with a semiclassical field of photons. Physicists can calculate the electromagnetic interactions between nuclei with the final result of the Weizsäcker-Williams approximation, Eq. 2.13. The photon flux in Eq. 2.13 provides the electromagnetic input to the $J/\psi$ photoproduction cross section calculation.

## 2.5   Vector Meson Dominance

The Vector Messon Dominace method for calculating the $J/\psi$ photoproduction cross section has three main components. VMD approach is constructed from the Weizsiäcker-Williams photon flux, the VMD fit to the proton-electron data, and the Glauber model for calculating the nuclear cross sections from the proton-electron cross sections. The Weizsiäcker-Williams photon flux provides the probe. The proton-electron scattering data combine with the Glauber model create a picture of the initial state of the nucleus. Each of the different approaches to calculating the UPC $J/\psi$ photoproduction cross section use these same elements. However, the different models each use the last two elements differently to produce different pictures of the nucleus and different cross

sections values.

The photon flux in the photoproduction cross section calculation must be finite in order for the cross section to be meaningful. The Weizsiäcker-Williams approximation, Eq. 2.13, produces a divergence at $b = 0$. The probability of the nuclei interacting would exceed one if the photon flux were infinite. The divergence that arises at $b = 0$ from $K_1$ results in an unphysically infinite photon flux. Removing the divergence is necessary. Special treatment of impact parameter, $b$, where the colliding nuclei overlap eliminates the divergence.

A modulation of the photon flux can subdue the divergence at $b = 0$. A convolution of the photon flux with the nucleon number density functions of the colliding nuclei produces the necessary modulation. Eq. 2.14 gives the nucleon density of a single nucleus,

$$\rho_A(s) = \frac{\rho_0}{1 + exp[(s - R_{WS})/d)]} \tag{2.14}$$

In Eq. 2.14, $s$ is the distance from the center of the nucleus, $R_{WS}$ is the radius of the nucleus, and $d$ is the skin depth, which determines how quickly the nucleon density falls off beyond the nuclear radius. In Eq. 2.15 the depth of the nucleus is integrated out leaving just the transverse dimension in $T_A$. The average number of nucleons in the overlap region is given by a convolution of $T_A$ from each of the two nuclei to produce $T_{AA}$.

$$T_A(\vec{r}) = \int dz \rho_A(\sqrt{|\vec{r}|^2 + z^2})$$
$$T_{AA}(|\vec{b}|) = \int d^2\vec{r} T_A(\vec{r}) T_A(\vec{r} - \vec{b}) \tag{2.15}$$

$T_{AA}$ is the function that modulates the photon flux. As input to the Poisson distribution, $T_{AA}$ reduces Eq. 2.13 at values of $b$ where the nuclei overlap significantly and eliminates the divergence in the photon flux.

Modulating the photon flux by the probability that no nucleon-nucleon collisions occur limits the photon flux at low $b$ in Eq. 2.13. The convolution of the photon flux with the $b$ dependent probability that no nucleon-nucleon collisions occur removes the divergence in Eq. 2.13. Using

the mean number of nucleons in the overlap region given by $T_{AA}$, the Poisson distribution gives the probability that no collisions occur at a given $b$:

$$P_0(b) = exp[-T_{AA}(b)\sigma_{NN}] \tag{2.16}$$

In Eq. 2.16, $\sigma_{NN}$ is the cross section for a nucleon-nucleon interaction, which gives the probability that a collision will occur given the average number of nucleons in the overlap region. The average photon flux over impact parameter, $b$, can be calculated from the integration of the $b$-dependent photon flux, Eq. 2.13, with the $b$-dependent probability of having no nucleon-nucleon interactions, Eq. 2.16.

$$\frac{dN_\gamma(k)}{dk} = \int_0^\infty 2\pi b db P_0(b) \int_0^R \frac{r dr}{\pi R_A^2} \int_0^{2\pi} d\phi \frac{d^3 N_\gamma(k, b + r\cos(\phi))}{dk d^2 r} \tag{2.17}$$

Eq. 2.17 goes down to $b = 0$ where the photon flux is infinite, but because the probability of having a nucleon-nucleon collisions is high, the divergence is eliminated. The result of Eq. 2.17 does not diverge.

A power-law fit to the proton photoproduction data gives an analytic expression for the energy dependence of the proton photoproduction cross section. The fitting function is simple and only depends on the photon-proton center of mass energy, $W$. Eq. 2.18 gives the parameterization of the forward proton photoproduction cross section fit.

$$\frac{d\sigma(\gamma p \to V p)}{dt}\bigg|_{t=0} = b_v(XW^\varepsilon + YW^{-\eta}) \tag{2.18}$$

$W$ is the center of mass energy of the proton-photon system in Eq. 2.18. The remaining variables in Eq. 2.18 are simple power-law fit parameters. The $XW^\varepsilon$ term characterizes pomeron mediated interactions, and the $YW^\eta$ term characterizes meson mediated interactions[8]. $J/\psi$'s high mass relative to the $\pi$ and $\rho$ renders the second term in Eq. 2.18 negligible as the term falls rapidly with increasing $W$. Eq. 2.18 allows for extrapolation and interpolation of the measured forward proton photoproduction cross section. The fit to the data provides estimates for energies that have not yet

been probed experimentally.

The proton-electron scattering data is used differently in the VMD method than in the other major methods. The VMD method for calculating UPC photoproduction cross sections relies more on electron-proton scattering data. The proton photoproduction cross sections from the electron-proton scattering data is a direct input to the VMD model. A power-law fit to the proton photoproduction data, as opposed to model dependent gluon densities of other approaches, combines with the Glauber model to provide the nuclear model in the VMD method. Because of the simplicity of the method, the VMD approach incorporates less modifications of the nuclear initial state relative to the proton initial state. As a result, the VMD method produces a higher UPC $J/\psi$ photoproduction cross section relative to the other methods.

Vector meson dominance and the optical theorem allow for the calculation of the total proton-meson scattering cross section from the fit given by Eq. 2.18. The optical theorem relates a total cross section, $\sigma$, to a corresponding forward scattering cross section, $d\sigma/dt|_{t=0}$. Vector meson dominance asserts that the colored part of the photon wave function is dominated by vector mesons; therefore, the photon is represented as a quark-antiquark pair in photoproduction calculations. These two components combine to produce Eq. 2.19.

$$\frac{d\sigma(\gamma p \to V p)}{dt}\bigg|_{t=0} = \frac{4\pi\alpha}{f_v^2(M_V, \Gamma_{l^+l^-})} \frac{d\sigma(V p \to V p)}{dt}\bigg|_{t=0}$$
$$\sigma(V p)_{tot}^2 = 16\pi \frac{d\sigma(V p \to V p)}{dt}\bigg|_{t=0} \tag{2.19}$$

In Eq. 2.19, the photon-proton scattering is related to meson-proton scattering through the photon-meson coupling, which depends on the vector meson's mass, $M_V$, and leptonic decay width, $\Gamma_{l^+l^-}$. The result of combining vector meson dominance and the optical theorem in Eq.2.19 provides the cross section for a meson to scatter off a proton. The total proton-meson scattering cross section, provides the input to the Glauber model calculation of the nuclear photoproduction cross section.

The nucleus-meson scattering cross section relates to Eq. 2.19 through the Glauber model. The Glauber model allows for Eq. 2.19, the proton-meson scattering cross section, to be used to

calculate a nucleus-meson scattering cross section. The Glauber model produces nuclear cross section calculations from nucleon (proton or neutron) interaction cross sections by use of $T_{AA}$. The combination of the mean number of nucleons in the overlapping region of a nucleus-nucleus collision, $T_{AA}$, the nucleon cross section, $\sigma$, and the Poisson distribution make-up the core of the Glauber model. For the total nucleus-meson scattering cross section, the equation has the following form:

$$\sigma_{tot}(VA) = \int d^2\vec{r}(1 - e^{-\sigma_{tot}(Vp)T_{AA}(\vec{r})})  \qquad (2.20)$$

In Eq. 2.20, the term $e^{\sigma_{tot}(Vp)T_{AA}}$ gives the probability of having no meson-nucleon scatterings from the Poisson distribution. The probability of having at least one scattering is given by subtracting one from the term $e^{\sigma_{tot}(Vp)T_{AA}}$ in Eq. 2.20. As seen in Eq. 2.20, the Glabuer model leverages scientific knowledge of the proton to understand of the nucleus. The Glauber model is the tool that combines the proton photoproduction data with nucleon distributions in the nucleus to produce a nuclear vector meson photoproduction cross section in the VMD approach.

Reversing the process used for the proton, Eq. 2.20, the meson nucleus scattering cross section, relates to forward nuclear photoproduction cross section through the optical theorem. The nuclear photoproduction cross section is the input to the calculation of the final result, the nuclear vector meson photoproduction cross section in UPC events. Eq. 2.21 uses the optical theorem to produce the nuclear photoproduction cross section from the nucleus-meson scattering cross section:

$$\frac{d\sigma(\gamma A \to VA)}{dt}\bigg|_{t=0} = \frac{\alpha\sigma_{tot}^2(VA)}{4\pi f_v^2}$$

$$\sigma(\gamma A \to VA) = \frac{d\sigma(\gamma A \to VA)}{dt}\bigg|_{t=0} \int_{t_{min}}^{\infty} dt |F(t)|^2  \qquad (2.21)$$

$F$ in equation Eq. 2.21 is the Fourier transform of the nuclear density function, $\rho_A$. To produce the formula for calculating the UPC vector meson photoproduction cross section, Eq. 2.21 is combined with the photon flux incident on the nucleus, Eq. 2.17.

$$\sigma(AA \to AAV) = 2 \int dk \frac{dN_\gamma}{dk} \sigma(\gamma A \to VA)  \qquad (2.22)$$

14

The factor of 2 in Eq. 2.22 comes from the fact that both of the two colliding nuclei contribute. Combining the three elements of VMD, Eq. 2.22 is the final result of the VMD UPC photoproduction cross section calculation. Vector meson production rates in UPC collisions are predicted by Eq. 2.22, which can be confirmed or denied by experiment.

## 2.6   Leading Twist Approach Derivation

The LTA method for calculating UPC photoproduction cross sections combines elements of the Glauber model with direct use of gluon densities. The proton gluon density is modified by a nuclear modification function in the LTA method to produce the nuclear gluon density. The nuclear modification function converts the proton photoproduction cross section to a nuclear photoproduction cross section in the LTA method. The LTA method is different from the other methods in its direct use of the nuclear modification factor and how the nuclear modification factor calculation incorporates multiple scattering. The direct use of the nuclear modification factor produces the most gluon shadowing out of the three major methods, and results in the lowest cross sections. The LTA method is the easiest to constrain experimentally for this reason.

The LTA method uses the Weizsiäcker-Williams approximation to calculate the photon flux created by the colliding nuclei. As in the VMD method, the probability of having no hadronic collisions modulates the flux. The photon flux for the LTA method has the following form [9]:

$$n^i_{\gamma/A}(\omega_\gamma) = \frac{2\alpha Z^2}{\pi} \int_{b_{min}}^{\infty} db \frac{x^2}{b} \left[ K_1^2(x) + \frac{K_0^2(x)}{\gamma_L^2} \right] P_0(b) P_C^i(b) \tag{2.23}$$

$$x = \frac{\omega b}{\gamma_L v}$$

The $K_0^2(x)$ term contributes a photon flux in the transverse direction. $P_C^i(b)$ is an additional modulation factor that requires various additional interactions. These interactions result in additional emissions of neutrons from the receding nuclei as the nuclei relax from excited states. The LTA flux reproduces the VMD result when the $K_0$ term becomes negligible as $\gamma_L$ approaches $\infty$ and

$P_C^i = 1$ when all emissions are allowed. The terms $P_C^i$ and $K_0$ create additional ways to distinguish UPC events from nuclear collisions experimentally but leave the underlying interaction mechanism the same. For example, the additional terms in the LTA formulation of the photon flux produce calculations of asymmetric neutron emission, which separate UPC events from nuclear collisions.

The LTA method calculates the nucleon photoproduction cross section from the nucleon gluon density. Ref. [9] derives the nucleon cross section from derivations of the nucleon gluon densities from electron-proton scattering data and leading order perturbative quantum field theory calculations. The forward photoproduction cross section of the nucleon has the following form [9]:

$$\frac{d\sigma_{\gamma N \rightarrow J/\psi N}(t=0)}{dt} = \frac{16\Gamma_{l^+l^-}\pi^3}{3\alpha M_{J/\psi}^5}[\alpha_s\mu^2 x G_N(x,\mu^2)]^2 \tag{2.24}$$

Here $G_N$ is the gluon density of the nucleon, $x$ is the fraction of the nucleon's momentum the gluon carries, and $\mu$ is related to momentum at which the nucleon is being probed, which is equal to $M_{J/\psi}/2$ for $J/\psi$ photoproduction. In Eq. 2.24 the nucleon cross section is explicitly connected to the gluon density. By connecting the gluon density to the cross section, Eq. 2.24 allows for the gluon density to be experimentally probed.

Ref. [9] exploits the optical theorem to relate the forward photoproduction cross section of the nucleon to the nuclear cross section. Eq. 2.25 gives the relation:

$$\sigma_{\gamma A \rightarrow J/\psi A}(\omega) = \frac{d\sigma_{\gamma N \rightarrow J/\psi N}}{dt}(\omega, t_{min})R_g^2 \int_{t_{min}}^{\infty} dt|F(t)|^2 \tag{2.25}$$

$$R_g = \frac{G_A(x,\mu^2)}{AG_N(x,\mu^2)}$$

$R_g$, the nuclear modification function, is the ratio between the gluon density of the nucleon, $G_N$, to the gluon density of the nucleus, $G_A$. As with the VMD method, the optical theorem relates the forward cross section, $\frac{d\sigma_{\gamma N \rightarrow J/\psi N}}{dt}(\omega, t_{min})$, to the total cross section, $\sigma_{\gamma A \rightarrow J/\psi A}$. The LTA method relates the measurable UPC photoproduction cross section to the gluon density of the nucleus. Eq. 2.25 further connects the gluon density of the nucleon to the relative reduction of the gluon

density in the nucleus through $R_g$.

From Eq. 2.25, the LTA method can predict the angular distribution of photoproduced $J/\psi$ with respect to the beam axis. In Ref. [10] the angular distribution is expressed in the form of the rapidity dependency of the UPC photoproduction cross section.

$$\frac{d\sigma_{A_1A_2\to A_1A_2J/\psi}}{dy} = n_{\gamma/A_1}(y)\sigma_{\gamma A_2\to J/\psi A_2}(y) + n_{\gamma/A_2}(-y)\sigma_{\gamma A_1\to J/\psi A_1}(-y) \qquad (2.26)$$

$$y = ln\left(\frac{2\omega}{M_{J/\psi}}\right)$$

Eq. 2.26 is comprised of two terms, one for photons from the forward going nucleus interacting with the backward going nucleus, and a second for the reverse situation. The integration of Eq. 2.26 over $y$ produces the factor of 2 that is present in Eq. 2.22. The rapidity distribution of the photoproduction cross section given in Eq. 2.26 provides a more detailed prediction and allows for more direct experimental comparison. Eq. 2.26 allows for comparison to rapidity regions that are covered by experiments.

The LTA method is distinct from the pQCD method and VMD method through the use $R_g$, the nuclear gluon modification factor. As opposed to using $R_g$, the pQCD method uses the nuclear gluon density, and VMD model uses proton photoproduction cross sections directly. In the LTA method, $R_g$ is calculated through a combination of $J/\psi$ photoproduction data from proton-electron scattering and DGLAP evolution equations, which incorporates nuclear multiple scattering effects [9]. The DGLAP evolution equations give the depends of nuclear gluon densities on the momentum scale at which the nucleus is probed, $\mu$ in Eq. 2.24. The unique way the LTA method calculates $R_g$ results in lower cross sections than the other major methods and allows for experimental sensitivity. Experimental measurements of the UPC $J/\psi$ photoprodcution cross section with CMS have the opportunity to distinguish whether $R_g$ as calculated in the LTA method accurately predicts the gluon density of the nucleus.

## 2.7 Perturbative Quantum Chromo-dynamics

To calculate the UPC $J/\psi$ photoproduction cross section, the pQCD method uses the nuclear gluon density to characterize the nucleus and the Weizsäcker-Williams approximation for the probing photon flux. The pQCD method combines these components such that the nuclear gluon density is a direct variable. The nuclear gluon density term in the pQCD formulation allows for the use of a variety of nuclear gluon density models. A range of nuclear gluon densities are present in the available models resulting in a wide range of cross section values. The UPC $J/\psi$ photoproduction cross section is correlated with the gluon density of the nucleus rising with higher densities and shrinking with lower densities. In the pQCD approach, the calculation of the UPC $J/\psi$ photoproduction cross section allows experiments to constrain many different nuclear gluon density models.

In the pQCD method, the photon interacts with the nucleus by fluctuating to a quark-anitquark pair. For $J/\psi$, the photon fluctuates to a $c\bar{c}$ pair. The probability for the photon to fluctuate to a $c\bar{c}$ pair depends on the $M_{J/\psi}$, the mass of $J/\psi$, $\Gamma_{l^+l^-}$, the $J/\psi$ leptonic decay width, and $\alpha$, the electromagnetic coupling constant. These three variables connect the c quark to the electromagnetic force mediator, the photon. Recast as a $c\bar{c}$ pair, the photon couples to the nuclear gluon density. Ref. [11] uses the fluctuation of the photon to a $c\bar{c}$ pair as the foundation for calculating the forward $J/\psi$ photoproduction cross section.

The $c\bar{c}$ pair arising from the photon fluctuation scatters off the gluons of the nucleus. The density of gluons in the nucleus determines how likely and therefore how large the cross section is for the quarks to scatter and form a $J/\psi$. The forward scattering cross section is the portion of those scattering events which transfer the minimum amount of momentum between the photon and the nucleus. The forward cross section for $J/\psi$ photoproduction in the nucleus has the following form [11]:

$$\frac{d\sigma_{\gamma A \rightarrow J/\psi A}}{dt}\bigg|_{t=0} = \xi_{J/\psi}\left(\frac{16\pi^3\alpha_s^2\Gamma_{l^+l^-}}{3\alpha M_{J/\psi}^5}\right)[xG_A(x,\mu^2)]^2 \tag{2.27}$$

In Eq. 2.27, $\xi_{J/\psi}$ is an experimentally derived correction factor, $\alpha_s$ is the strong coupling constant,

$x$ is the momentum faction of the nucleus the scattering gluons carry, and $G_A$ is the gluon density of the nucleus. Both the $c$ and $\bar{c}$ couple to the gluon density, and the double coupling results in the squared dependence of the cross section on the gluon density in Eq. 2.27. Fitting Eq. 2.27 to proton-electron scattering data sets $\xi_{J/\psi}$ [11]. The forward scattering cross section given by Eq. 2.27 connects the photon flux to the gluon density and provides the input to calculate the total cross section by the optical theorem. Eq. 2.27 is the crux of how UPC measurements provide insight into the gluon content of the nucleus.

The optical theorem relates the forward cross section in Eq. 2.27 to the total photoproduction cross section. The total cross section calculated by use of the optical theorem gives the probability that a photon incident on the nucleus will produce a $J/\psi$ regardless of the momentum transfered in the interaction. Ref. [11] gives the form of the total cross section equation:

$$\sigma_{\gamma A \to J/\psi A}(k) = \frac{d\sigma_{\gamma A \to J/\psi A}}{dt}\bigg|_{t=0} \int_{t_{min}(k)}^{\infty} dt |F(t)|^2 \tag{2.28}$$

Here $t_{min} = (M^2_{J/\psi}/4k\gamma_L)^2$, which is the minimum amount of momentum transfer required to produce a $J/\psi$ given the photon wave number $k$. The $k$ dependence of $t_{min}$ produces the rapidity, $y$, dependence of the total cross section. The total cross section for photoproduction, Eq. 2.28, provides the input to Eq. 2.26, which gives the rapidity dependence of the UPC photoproduction cross section. Eq. 2.28 as input to Eq. 2.26 allows for experimental comparison of the pQCD method to measurements of UPC photoproduction cross sections. With the pQCD method's direct use of the nuclear gluon density in Eq. 2.27, the pQCD method allows for experimental exploration of any gluon density model.

## 2.8   Incoherent Photoproduction

## 2.9   Photon Induced Nuclear Break-up

Two different approaches are discussed. The first is to measure the desired cross-section directly. This can be done by bombarding the target material with mono-energetic real photons, varying the energies of the photons over a range of frequencies, and extrapolating that data up to the photon energies that arise in the Weizäcker-Williams approximation [3]. The other approach is to create a theoretical model of how the target reacts to a photon flux [4]. In the theoretical model that will be discussed in this paper, the photonuclear cross-section, the cross-section governing the absorption of photons by a nucleus, is formulated as the sum of two other cross-sections that are known better. In both, the more detailed theoretical approach and the empirical approach to the problem, the interaction of the Weizäcker-Williams quasi-real photons is assumed to be identical to the interaction of real photons with the target.

To model the interaction of the photons with the target nuclei, as done in Ref. [4], the photonuclear cross-section is broken down into two parts.

(16) The Giant Dipole Resonance (GDR) cross-section dominates at lower photon frequencies and is the result of the collective motion of the protons relative to the neutrons. The Quasi-Deuterium (QD) cross-section dominates at higher photon energies and is the result of treating the nucleus as a collection of proton-neutron pairs, which is deuterium.

The giant dipole resonance has been studied for decades. In 1947, Baldwin and Klaiber first observed the giant dipole resonance [6]. At the General Electric Research Laboratory, Baldwin and Klaiber found that by bombarding a uranium target with photons in the range $10 - 100$ MeV, a peak in the spectrum was found for photons at 20 MeV. A year later, Goldhaber and Teller theorized that this was the result of the protons moving back and forth with respect to the neutrons [6]. In this model, the protons and neutrons are treated as two separate liquid dots. Then in 1950, Steinwedel and Jensen modified this theory by modeling the protons and neutrons as fluids contained in a single sphere rather than two separate dots moving back and forth [6].

In order to understand the Goldhaber and Teller model, it is useful to consider a nucleus where the number of protons and neutrons are equal, Z=A/2. The collection of protons and the collection of neutrons move opposite each other and only in the z direction. In order to construct a Hamiltonian, first the kinetic energy should be considered.

(17) Eq. 17 is the familiar equation for kinetic energy simply summed over all the constituent nucleons of the nucleus. The protons and neutrons are modeled as separate liquid drops with densities $\rho$p and $\rho$n. These liquid dots will oscillate back and forth in opposite phase relative to the center of mass maintaining there individual density profiles.

The potential holding protons and neutrons together depends on the difference of the two densities squared. If the two exactly overlap, there is no difference in the densities and the potential energy is zero. If the two density distributions are separated, there will be regions where the neutron density is greater and regions where the proton density is greater. In the separated configuration, there will be potential energy. The potential energy can be shown to have the form of a harmonic oscillator with a spring constant that depends on the initial density distribution [6].

(18) If the nucleus has a shape cut off in density at it's very edge, then the integral is dominated by the region at the surface, and the spring constant K becomes proportional to the mass number to the 2/3rds power, A2/3. This is the consequence of the of geometry of a sphere. The surface area of a sphere is proportional to its volume to the 2/3rds power. Recalling the angular frequency of a harmonic oscillator, (19) it is seen that the frequency of the giant dipole resonance in the Goldhaber and Teller model is proportional to the mass number to the negative 1/6th power, A-1/6. This dependence describes light nuclei well, but it does not describe heavier nuclei [6].

In order to describe heavier nuclei, the Steinwedel and Jensen model must be used. In the Steinwedel and Jensen model, the proton and neutron fluids are confined to a single sphere where they are allowed to slosh back and forth creating the same effect as the Goldhaber and Teller model. In this model, there is no global separation of the proton and neutron fluids. The dipole is created by underdensities and overdensities of the proton and neutron fluids. It can be shown that this results in a frequency of oscillation which depends on one over the radius of the nucleus [6]: (20)

As before, the relationship in Eq. 20 arises from the geometry of a sphere. The dependence of the giant dipole resonance that is seen in the Steinwedel and Jensen describes medium and heavier mass nuclei well. Empirically, both models are stitched together to give the following mass number dependence of the peak dipole resonance [6].

(21) In order to compute the effect of an excitation in either model, the harmonic oscillator solutions found earlier can be driven by an interacting force. The resulting differential equation can then be solved using a Fourier transform to eliminate the time derivatives and reduce the equation to an algebraic equation. Following this procedure produces the shape of energy dependence of the giant dipole resonance, and this gives a cross-section for photon absorption by the giant dipole resonance with Lorentzian form [6]: (22) here $\sigma$max is the maximum cross-section, when E$\gamma$g = EGDR, EGDR is the peak resonance energy, and $\Gamma$GDR is the width of the resonance. The width, $\Gamma$GDR, of this distribution lies in a range from 4-8 MeV and depends on the orbital arrangement to the neutrons and protons in the given nucleus [6].

For higher energy photons, the quasi-deuterium cross-section is needed. The quasi-deuterium approach amounts to treating the nucleus as a bunch of proton-neutron pairs, which are screened by the rest of the nucleus. Eq. 23 models this behavior [4].

(23) Here $\sigma$d is the deuterium disintegration cross-section for $\gamma$g+d $\rightarrow$ p+n. F is a function that arising from Pauli blocking of fermions, and L is an empirical parameter set by data that is equal to 6.5. Certain energy levels are not available to the products of the deuterium disintegration process because of the presence of the rest of the nucleus. The result is a reduction of the cross-section.

F can be modeled with an exponential cutoff below 20 MeV, a polynomial in the intermediate range with nearly linear dependence on E$\gamma$g, and above 140 MeV an inverted exponential pushing F to one at higher values of E$\gamma$g [4]. Essentially, the model at low photon energies disallows deuterium disintegration because the products have no available state to occupy, and at high energies the rest of the nucleus becomes transparent and looks more and more like a collection of deuterium. The deuterium disintegration cross-section is found empirically and is fit to the following function [4]: (24) In order to produce a final state for the target nucleus, a branching ratio is

needed. The branching ratio gives the probability that the photo-excited nucleus will end up in a particular state. This determines the sort of emission that will result from the de-excitation process. There are two phases of deexcitation, the nonequlibrium phase and the equilibrium phase. In the time before reaching equilibrium, fast nucleons are emitted. Subsequently, in the equilibrium phase, slow nucleons evaporate. These two phases are simulated in complex computer codes that calculate branching ratios (see discussion in Ref. [4]).

All the tools are now assembled to calculate the cross-section for any particular electromagnetic dissociation process. The first step in the calculation is to assume that the number of photons absorbed by either nucleus in the collision obeys the Poisson distribution [3,4]. An average number of absorptions is calculated and used in the construction of the distribution.

(25) When using the model of Ref. [4], the cross-section involved in Eq. 25 will be the photonuclear cross-section, and the calculation will produce the average number of photons absorbed by the target. If instead the empirically measured photoneutron cross-section is used as in Ref. [3], the mean calculated in Eq. 25 will be the number of photons absorbed that result in neutron emission from the target. This restricts the calculation to only de-excitation modes that produce neutrons. Both averages are for a given impact parameter b.

Following Ref. [3] and using the experimentally measured photoneutron cross-section, the probability Pn for the target to produce a number of neutrons, k, due to the photon flux of the projectile can be calculated using Eq. 26.

(26) This is just the Poisson distribution. In the collider situation, where both nuclei can be treated as the target and the projectile, the probability of mutual emission, one nucleus emitting x neutrons and the other emitting y neutrons, can be calculated from Eq 27.

(27) It is also interesting to consider the situation where at least one neutron is emitted. This can be calculated by subtracting the probability of no neutrons being emitted from one.

When using the model of Ref. [4], a branching ratio is needed to calculate the probability of de-exciting into a given state. The probability of photon absorption is calculated as in Eq. 26, only using the model of Ref. [4]. This is the probability of the target absorbing k photons rather than

then the nucleus absorbing a photon and emitting a neutron. In Ref. [4], the probability of any final state i due to the absorption of a single photon can be calculated using Eq. 28.

(28) Here Pa is the probability that the target absorbs a single photon as calculated by Eq. 26, q is the probability that the photon will have the frequency $\omega$, and fi is the branching ratio. The following equation describes q [5].

(29) By multiplying Eq. 26 and 29 in Eq. 28, the m(b) terms cancel and produce a simplified equation. The forms for probability functions, like Eq. 28, that involve absorption of multiple photons have additional terms. But they follow that same scheme of multiplying the probability of absorption times the probability that the absorbed photon has a particular frequency times the branching ratio.

The probability functions Eq. 26 and Eq. 28 can than be used to produce cross-sections. For any given process, using Eq. 28 can be used by inserting the appropriate branching ratio. For emission of neutrons, Eq. 26 can be used. This is done by integrating over the impact parameter to get an area that is weighted by the probability functions [3,4].

(30) If the branching ratio for neutron emission is selected in Eq. 28, then Eq. 28 and Eq. 26 can be used to compute the same cross-section through the use of Eq. 30.

Three parameters arise when calculating the cross-section in Eq. 30, the minimum impact parameter bo, the minimum emitted photon frequency $\omega$min, and the maximum emitted photon frequency $\omega$max. The need for a minimum impact parameter is necessitated by the Bessel function in the photon flux in Eq. 14. At zero, the modified Bessel function does not converge. Physically, a minimum impact parameter is selected in order to separate the domains between electromagnetic interactions and the strong interactions that happen inside the nucleus. To serve this end, the minimum impact parameter is set to the radius of the nuclei [3,4]. This excludes collisions where the nuclei overlap in the calculation, and assures only electromagnetic interactions are involved.

| Model | $\sigma_{AA \to AAJ/\psi}(mb)$ |
|---|---|
| VMD/STARlight MC | 23 |
| LTA | 9 |
| pQCD-MSTW08 | 34 |
| pQCD-EPS08 | 7 |
| pQCD-EPS09 | 14 |
| pQCD-HKN07 | 23 |

Table 2.1: $\sigma_{AA \to AAJ/\psi}(mb)$ the LTA, VMD, pQCD methods. Four different gluon density models are used in the pQCD method. STARlight is a simulation software package that utilizes the VMD model.

## 2.10   Theoretical Results

The UPC photoproduction cross section calculations depend significantly on how the nucleus is represented in the calculation. The results from the VMD, LTA, and pQCD methods vary from a relatively large cross section in the VMD model, ranging through a variety of values in the pQCD method, to a relatively small cross section in the LTA method. Each of these methods utilizes the same probe of the nucleus, the equivalent photon flux that is calculated using the Weizsiäcker-Williams approximation. The three methods deviate in how they calculate the forward photo-production scattering cross section. The differences in the UPC photoproduction cross sections predicted by the different models demonstrates the amount of experimental sensitivity there is to distinguishing between the models. The dependence of the cross section on rapidity shows where in phase space a measurement of the cross section is most sensitive.

The predicted value for the UPC $J/\psi$ photoproduction cross section in PbPb collisions at the LHC differ widely depending on which of the three main methods is used. The cross section value calculated by Eq. 2.22 in the VMD, LTA, and the various gluon density models in pQCD method vary significantly. Table 2.1 gives the predicted values for the three main methods taken from Ref [12], Ref [9], and Ref [8]. The cross sections in Table 2.1 differ by a factor of $\approx 4$ from the smallest to largest and create an experimental opportunity. The clear discrepancy between the models in Table 2.1 demonstrates the high amount of experimental sensitivity there is for distinguishing between the models.

The rapidity dependence of the cross sections determine which values of rapidity will be most sensitive to differences in the models. The rapidity dependence calculated by Eq. 2.26 overlap between the models at certain values of $y$ leaving the models indistinguishable at that rapidity. Fig. 2.4 [13] shows the rapidity dependency of the UPC $J/\psi$ photoproduction cross section for the three main models including several different gluon density models using the pQCD method. In
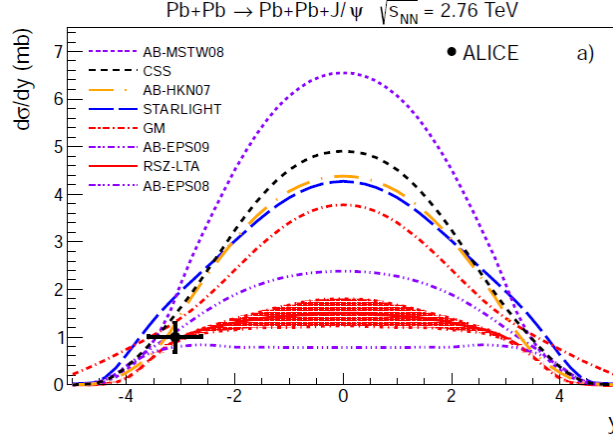


Figure 2.4: AB is the pQCD method, RSZ-LTA is the LTA method, and STARlight is the VMD model.

Fig. 2.4 at higher rapidities, in particular $|y| > 3$, the various models give similar values for $d\sigma/dy$. At $y = 0$ the models vary the most. Fig. 2.4 shows that experiments that can measure $J/\psi$ at $y = 0$ have the best opportunity to distinguish between the models. The high sensitivity at $y = 0$ creates an advantage for experiments that can measure particles with small rapidity and low momentum.

The UPC photoproduction models each have different shapes to their rapidity dependence. The slope of $d\sigma/dy$ in Fig. 2.4 depends on the model. Through the rapidity region $1 < |y| < 3$, each of the models has a progressively steeper slope. The LTA method and the pQCD method utilizing the EPS08 gluon density model are relatively flat where as the VMD and other gluon density models using the pQCD method have a noticeable slope. The differing slopes provide an additional experimental observable. The shape of the rapidity distributions provide experimental sensitivity at rapidities away from $y = 0$ and creates an opportunity for experiments that can not measure $J/\psi$ at $y = 0$.

The nuclear suppression factor, S, demonstrates the difference between how the models represent the nucleus. S, which is a ratio between the nuclear photoproduction cross section and the free nucleon photoproduction cross seciton, is a measure of how the nuclear gluon densities evolve in each of the models. Fig. 2.5 from Ref.[14] shows the nuclear suppression, which is equivalent to $R_g$ in Eq. 2.25, for the LTA and pQCD method. Fig. 2.6 shows the nuclear suppression for
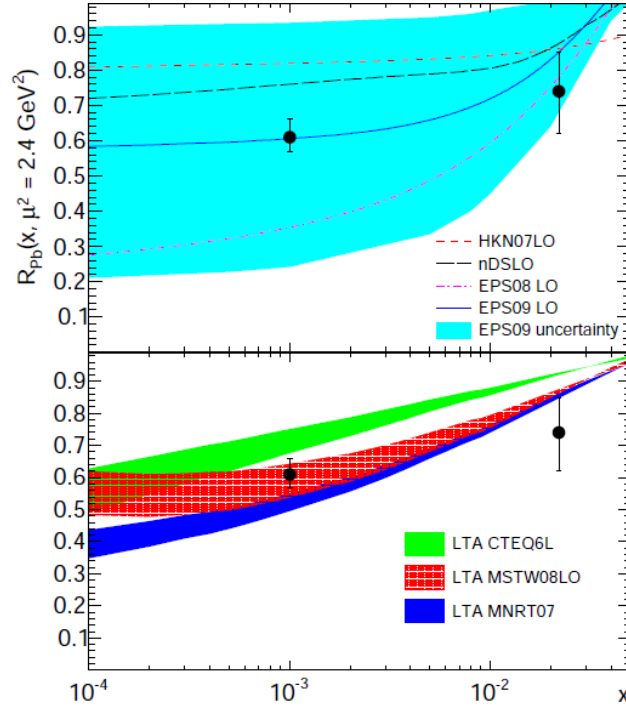


Figure 2.5: Nuclear supression factor, *S*, in the pQCD and LTA methods.

the VMD method [14]. Fig. 2.6 and Fig. 2.5 show that as the momentum of the probing photon goes up, increasing $W_{\gamma p}$, and momentum of the probed gluon goes down, decreasing $x$, the nuclear gluon density decreases relative to the free nucleon. The nuclear suppression factor, S, allows for the different models' representations of the gluon content of the nucleus to be directly compared to each other and to data. S can be measured from data by assuming a Weizsiäcker-Williams photon flux and provides insight into nuclear gluon densities.
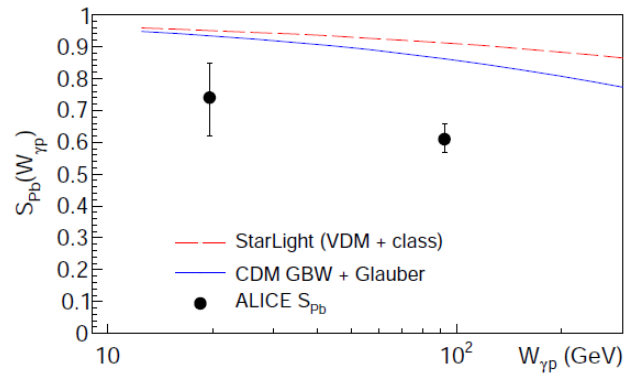
Figure 2.6: Nuclear supression factor, *S*, in VMD method.

# Chapter 3

# The CMS Detector

CMS is housed at interaction point 5 of the LHC. The LHC is designed to pursue physics at the TeV scale. This is the scale where electroweak symmetry breaking is believed to occur [**?**]. While this means that the search for the standard model Higs is the central driving design consideration, the wide range of possibilities for finding new physics signals requires a general purpose detector. The expedient discovery of new physics through low cross section interactions requires high luminosity. This consideration leads inevitably to pile up, where multiple collisions occurs at a single bunch crossing. At peak luminosity the LHC is expected to produce on average 20 hard proton-proton (pp) collisions per bunch crossing [2]. These particle physics considerations of high multiplicity due to pileup and the need for a general purpose detector make CMS serendipitously well suited for heavy ion physics.

The general purpose design of CMS is dominated by the massive 4T superconducting solenoid at its core. The magnets is 13m long with a 6m diameter, and pushes the limits of power and compactness [2]. These two conflicting limits are achieved through the novel design of interweaving structural and conducting elements together in the coil of the solenoid.

Within the solenoid resides three different sub detectors. The inner most is the world's largest silicon tracker [2]. The tracker is surrounded by a highly effective lead tungstate crystal electromagnetic calorimeter (ECAL). ECAL is encapsulated in a brass scintillating hadronic calorimeter
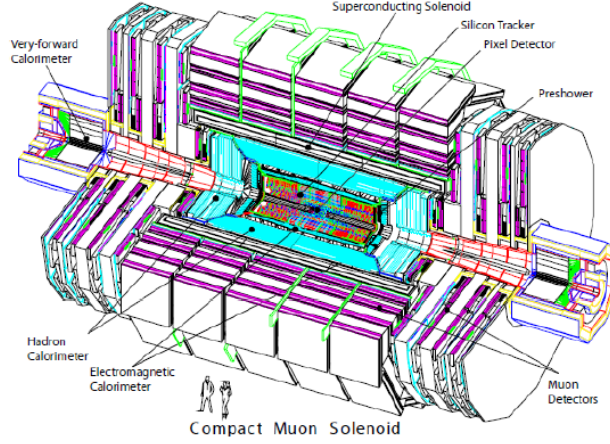
Figure 3.1: The Compact Muon Solenoid from Reference [2].

(HCAL). Outside the magnet, muon chambers are used to aid in the measurement and triggering of muon events. Altogether CMS weighs 12,500 metric tons, has a diameter of 14.6m, and a length of 21.6m [2].

The Silicon Tracker is the innermost sub-detector of CMS, and has active elements as close as 4.4cm to the interaction point [2]. The tracker has a length 5.8m, a diameter of 2.6m and covers a range in pseudorapidity of $|\eta| < 2.5$. Pseudorapidity is defined as $\eta \equiv -\ln(\tan(\theta/2))$, where $\theta$ is the polar angle, and $\phi$ is the azimuthal angle with respect to the beam axis. At the center of the tracker are three rings of silicon pixels around the beam with two disks of silicon pixels to cap the rings. The pixel portion of the silicon tracker is comprised of $66\times10^6$ pixels. The silicon pixels are surrounded by silicon strips. The silicon strips are separated into 4 different sections: the Tracker Inner Barrel, the Tracker Inner Disk, the Tracker Outer Barrel, and the Tracker End Caps. The silicon strip detectors as a whole are comprised of $9.3\times10^6$ silicon strips. The high number of pixels and strips allow for the ability to distinguish and collect enough distinct points to reconstruct the path of the 1000 or so charge particles per bunch crossing expected at peak luminosity [2].

The next detector beyond the tracker is ECAL. ECAL is made of 61,200 lead tungstate ($PbWO_4$) crystals in the central barrel and 7,324 on each of the two endcaps [2]. The barrel (EB) covers a pseudorapidity range $|\eta| < 1.479$ and has an approximate $\eta - \phi$ segmentation of $0.0174 \times 0.0174$. Lead tungstate is very dense, which is reflect in the high number of interaction lengths the short

depth of one crystal provides. The crystals of the barrel have a depth of 230 mm corresponding to 25.8 radiation lengths ($X_0$). The radiation length is the mean distance a high energy particle travels before giving up one e-fold of kinetic energy through electromagnetic interactions. For example, after one radiation length $E \rightarrow E/e$, where $e = 2.71828183$. The endcaps (EE) cover the psuedo-rapitity region $1.479 < |\eta| < 3$. In the endcap the crystals have an exposed area of $28.62 \times 28.62$ mm$^2$, and a depth of 220 mm corresponding to 24.7 $X_0$. The energy resolution of the ECAL as measured by test beam data can be seen in Figure 3.2.
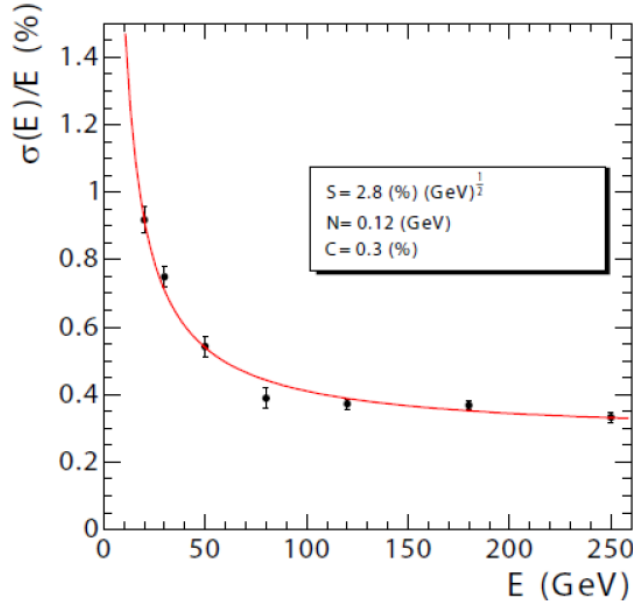


Figure 3.2: The energy resolution of ECAL as a function of energy from Reference [2].

The HCAL like the ECAL has both a barrel (HB) and endcaps (HE). The pseudorapidity region $|\eta| < 1.3$ is covered by HB [2]. HB has an $\eta - \phi$ segmentation of $0.0897 \times 0.0897$, and is 25 times more sparsely granulated than EB. HE covers the pseudorapidity region $1.3 < |\eta| < 3$. HE, like EE and the tracker endcaps, is aligned perpendicular to the beam axis resulting in granularity that changes with $\eta$. In the region $1.3 < |\eta| < 1.6$ HE has an $\eta - \phi$ segmentation of $0.0897 \times 0.0897$. The $\eta - \phi$ segmentation roughly doubles to $0.17 \times 0.17$ in the region $1.6 < |\eta| < 3$. The energy resolution of the barrel and endcaps can be seen in Figure 3.3. The thickness of the hadronic calorimeter is best described in interaction lengths, the mean distance for a particle to give up an e-fold of energy through nuclear interactions. At $\eta = 0$ the barrel has a thickness 5.82 interaction

lengths ($\lambda_I$), and increases as the path length through the material increases to 10.6 $\lambda_I$ at $|\eta| = 1.3$.
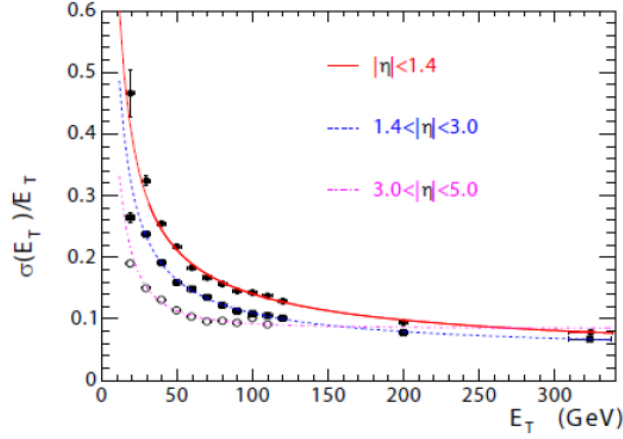


Figure 3.3: The $E_T$ resolution of HCAL as a function of $|\eta|$ and $E_T$ from Reference [2].

In addition to HB and HE, HCAL has two additional calorimeters. Because the space between ECAL and the magnet is restricted to 1.18 m, an outer hadronic calorimeter section (HO) is placed beyond the magnet in the region $|\eta| < 1.3$ [2]. The main function of HO is to collect energy from the highest energy hadrons before they reach the muon system. HO is not used in this analysis, but does contribute to the material budget. To increase the total calorimetric coverage, HCAL also has a quartz fiber calorimeter (HF) in the forward region, $3 < |\eta| < 5$. For the majority of HF's 13 $\eta$ rings the $\eta - \phi$ segmentation is $0.175 \times 0.175$. In the lowest $|\eta|$ ring the segmentation is $0.111 \times 0.175$ in $\eta - \phi$. In the highest two $|\eta|$ rings the segmentation in $\phi$ is 0.349, with an $\eta$ segmentation of 0.175 in the outer and 0.300 in the innermost ring. The longitudinal direction is effectively segmented by using short fibers and long fibers. The measure energy deposited deeper than 22 cm is measured in both the short and long fibers, where as the long fibers are present throughout. This allows electromagnetic showers to be distinguished from purely hadronic showers [2]. The energy resolution for HF can be seen in Figure 3.3.

Beyond HF there are two more detectors in the forward region. CASTOR covers the range 5.2 $< \eta < 6.6$ on the positive side of the beam. The Zero Degree Calorimeters (ZDC) sit between the beam pipes on either side of the interaction point covering the area around $\theta = 0$, $|\eta| > 8.3$. In

32

heavy ion collisions the ZDC has the ability to measure neutral particles that do not participate in the collision [2]. CASTOR extends the total coverage of the CMS as whole giving more access to low-x physics [2].

The ZDC has a total of 18 channels. Half of these 18 channels are on either side of the interaction point. The 9 channels on the side of CMS that correspond to positive $\eta$ are denoted $ZDC^+$, where as the 9 channels on the negative side are denoted $ZDC^-$. The 9 channels on each side are further sub-divided into an electro-magnetic (EM) section and a hadronic (HAD) section. The EM section is positioned in front of the HAD section with respect to the interaction point and is segmented transverse to the beam direction. The 5 EM sections are positioned in front to absorb the energy from electro-magnetically induced showers, which develop over a shorter distance than hadronically induced showers. The transverse segmentation allows for a measurement of the transverse shower width and the size of the beam spot at the ZDC. The HAD section is segmented in the direction of the beam and consists of 4 channels. The longitudinal segmentation allows for absorption of the full extended hadronic shower and the ability to measure the longitudinal shower shape.

Each the 18 channels contains a tungsten target and quartz fibers. The dense tungsten target is used to initiate the shower. The quartz fibers shine Cerenkov light as the high momentum charged particles from the shower pass through it. the light from the quartz fibers is channeled to photo-multiplier tubes, one for each ZDC channel. Through a cascade of photon induced electrical discharges, the photo-multiplier converts the Cerenkov light to an electrical pulse.

This electrical pulse travels $\sim 200$ m down a coaxial cable from the LHC tunnel to the counting house in the CMS service cavern. There the electrical pulse is digitized by the Charge Integrator and Encoder (QIE). The QIE integrates the current each 25 nano seconds. The charge is than mapped logarithmically to the 128 bits. This bit is sent across a small fiber optic cable to the HTR firmware card. Here each 25 ns signal is stored in a 250 ns buffer, and the timing is sync with the rest of the detector to insure the ZDC signal arrives at the central data acquisition system at the same time as the other sub detectors from the same collision.

The muon system resides just outside of the superconducting magnet. It consists of three complementary systems: drift tube (DT) chambers in the barrel, cathode strip chambers (CSC) in the endcaps, and resistive plate chambers (RPC) in both the barrel and endcap regions [2]. Ultimately the muon system is most useful for triggering on muons [2].

The heavy ion community is making use of the capabilities of CMS in a myriad of ways. The muon trigger has been used in the search for suppression of quarkonium states. This is an important probe of the correlation length within the hot dense state known as the quark gluon plasma (QGP). The tracker has been utilized for to study charged particle multiplicities, and and elliptical flow, two probes of the thermal expansion of the QGP. HCAL has aided in measuring jet suppression, which probes the strength with which the QGP interacts with strong interacting objects. Through its general purpose design and its ability to handle the high multiplicities produce by the LHC, CMS proves to be an excellent detector for investigating strongly interacting mater through heavy ion collisions.

## 3.1  Trigger

The CMS trigger is two teired. The L1 trigger is the lower level hardward based system. The High Level Trigger (HLT) is software base and runs on a computer farm at point 5 where CMS is housed.

# Chapter 4

# Analysis

## 4.1  MC Simulation

Every physical measurement is the product of the underlaying physics convolved with the response of the detector used to do the measurement. In order to understand the underlaying physical process, the detector's effect on the measurement must be understood and accounted for. As instruments become more and more complicated, the interplay between all of the many parts of the detector makes an analytic approach to the problem untenable. For this reason, the numerical technique of Monte Carlo (MC) simulation is the most useful approach.

MC simulations use random number generation to solve the problem numerically by brute force. First, particles are generated according the theoretical distributions. These particles are then propagated through a simulation of the detector. As the particles pass through the detector, random numbers are again used to determine how these particles interact with the materials of the detector based on the known properties of the material. In this way, the theoretical distributions are merged with the complicated response of the detector. The collective combination of the many sub detectors responses with the theoretical distributions emerges from the successive creation of random events. The result is the convolved response of the detector with the underlaying physical process that is to be studied.

In this thesis, two main classes of MC simulation samples were used. The first class uses STARlight to generate events. This class of MC samples corresponds to the theoretical calculations described in in Section 2.5. There are three different physical process described. Coherent $J/\psi$ production, where the photon couples to the nucleus as a whole, incoherent $J/\psi$ production, where the photon couples to a nucleon within the nucleus, and photon-photon process, where the photons from the two nuclei interact with each other to produce a lepton pair directly. All three STARlight sample produce a $\mu^+$ and $\mu^-$ in the final state that interacts with the detector. The second class uses PYTHIA6 to decay $J/\psi$s with a given input $p_T$ and rapidity distribution. Two samples of this class of particle gun data were produced each with different $p_T$ distributions (See Fig.).

The software chain used for producing the STARlight samples has five steps. Because STARlight is not integrated into the standard CMS software framework, this chain was developed for the analysis described in this thesis. First, STARlight is run in the specified mode, and a single file is created for each physics process, for this thesis, one file for the coherent process, the incoherent process, and the photon-photon process. The output from the STARlight generator is in a format specific to STARlight, therefore, the output from the original generation step is then converted to the Les Houches (LHE) format. In this conversion to LHE format, either the parent $J/\psi$ for the $J/\psi$ production samples, or the initial photon-photon pair are added LHE output file. The standard STARlight output only includes the final state particles. Additionally, the initial output from STARlight is split into a collection of smaller LHE files so that each the smaller samples can be processed in parallel. Each of the LHE files was then used as input to the CMS software frame work (CMSSW). The three remaining steps take place within the frame work. First the generated particles are propagated through the GEANT4 detector simulation. This accounts for all the interactions with the detector and produces as output a format identical to the raw data that is recorded during data taking. The next two steps are identical to data taking. The reconstruction software used during data taking is run on the output of the detector simulation, and last, the output of the reconstruction is reduced to the information that is needed for the final analysis.

The particle gun samples were created entirely within CMSSW. An interface to PYTHIA6 is

included within CMSSW, which takes the J/$\psi$ $p_T$ and rapidity distributions as input. The J/$\psi$ are created according to the input distributions and then uses PYTHIA6 to $\mu^+$ and $\mu^-$. As with the STARlight samples these muons are propagated through the GEANT4 simulation of the detector, and the raw data is produced. The remaining steps of running the reconstruction code and reducing the data to the final data needed for the analysis is identical to the STARlight production.

The five MC samples, three STARlight samples, and two particle gun samples, differ primarily in the $p_T$ distribution of the J/$\psi$s produced and the polarization of the J/$\psi$s, which effects angle at which the muon daughters are emitted relative to the direction in which the J/$\psi$ is traveling. In Fig.GenPtDist the $p_T$ of J/$\psi$ for the coherent and photon-photon samples are peaked steeply a low $p_T$, and neither sample extends much beyond 0.15 GeV in $p_T$. The incoherent sample is peaked near 0.5 GeV and extends beyond 1 GeV. The two particle gun samples resemble the incoherent and coherent samples. The first sample has a Gaussian $p_T$ distribution extending to approximately 0.15 GeV, whereas the second is flat in $p_T$ up to 2 GeV. The particle gun samples are unpolarized, whereas the STARlight samples have transverse polarization. Therefor the particle gun samples there is no preferred direction for the emission of the daughter muons. In the STARlight samples however the daughters tend to be emitted in line with the direction of the motion of the J/$\psi$. This is particularly pronounced for the photon-photon process.
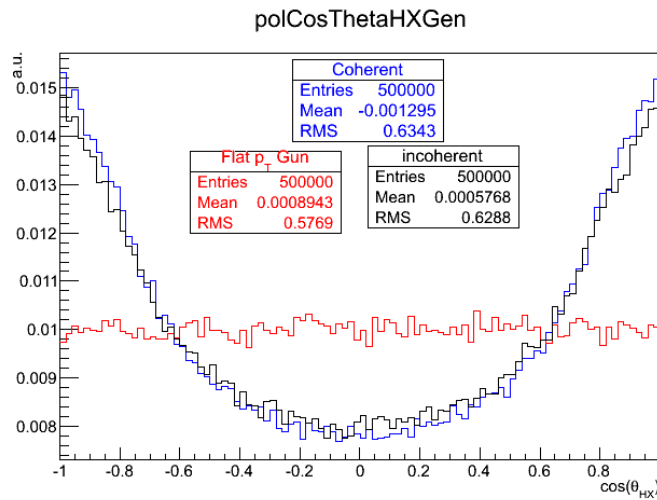


Figure 4.1: The J/$\psi$ polarization of the particle gun , coherent, and incoherent samples are plotted as the cosine of the helicity angle.

## 4.2    Trigger Development

Prior to the 2011 LHC PbPb run, UPC events had not been directly studied in PbPb collisions using CMS. Design of the UPC triggers required studies of the 2010 data to estimate rates and insure that the bandwidth used by these trigger would be sufficiently low. All the different physics analyses must share the limited readout rate of the detector. For this reason, conservation of bandwidth was a major design consideration.

To estimate the 2011 rates prior to the run, the 2010 rates were used to extrapolate to the interaction rate of the 2011 run. The unique UPC triggers were estimated by combining existing triggers from the 2010 run. By calculating the ratio between the UPC trigger rates and the minimum bias trigger rate, the UPC trigger rates were scaled up to the 2011 interaction rates using the 2010 data. The extrapolated rates allowed for a package triggers to be created, which fit within the bandwidth requirement of CMS Heavy Ions.

The trigger package for 2011 contained ZDC based efficiency monitoring triggers, muon and electron based triggers for measuring $J/\psi$, and backup triggers in case there was a problem with the original muon and electron triggers. In order to recorded the trigger efficiency monitoring data, the ZDC triggers had to be prescaled to a lower rate. The scaling down of the monitoring triggers were setup to insure overlap with the signal triggers. By balancing the competing objectives of rate reduction and increasing the overlap between the monitoring and signal triggers, the prescales for the trigger were as seen in Table .

### 4.2.1    L1 Trigger

The goal of the L1 triggers was to record enough data to measure dimuons and dielectrons in UPC events. To achieve this, the loosest muon trigger and lowest threshold ECAL triggers where paired with a trigger on energy in the ZDC and a veto on energy in the BSC or HF. The L1 package that was constructed for the analysis of UPC $J/\psi$ is presented in Table 4.1.

The cumulative L1 trigger rate for all the UPC L1 trigger seeds was required to be 200 Hz. This

| L1 Trigger Seed | Type |
|---|---|
| L1_MuOpen_ZdcCalo_NotBscMinBiasThresh2_BptxAND | Physics |
| L1_EG2_ZdcCalo_NotBscMinBiasThresh2_BptxAND | Physics |
| L1_EG5_ZdcCalo_NotBscMinBiasThresh2_BptxAND | Physics |
| L1_ZdcCaloMinus_BptxAND | Monitor |
| L1_ZdcCaloMinus_BptxAND | Monitor |
| L1_MuOpen_ZdcCalo_NotHcalHfCoincidencePm_BptxAND | Backup |
| L1_EG2_ZdcCalo_NotHcalHfCoincidencePm_BptxAND | Backup |
| L1_EG5_ZdcCalo_NotHcalHfCoincidencePm_BptxAND | Backup |

Table 4.1: List of 2011 L1 seeds.

requirement stemmed from the need to keep the tracker read-out rate low. The trackers baseline voltage can fluctuate due to the high tracker hit multiplicities in PbPb collisions. In order to monitor the zero suppression of the tracker, the zero suppression algorithm was executed using the HLT computing farm rather than the in the tracker firmware. The additional computing cycles needed to run the zero suppression the limit for L1 bandwidth.

## 4.2.2 HLT Trigger

As opposed to the L1 trigger, which reads out the tracker, the HLT has access to the tracker information. Reconstruction of a track in the pixel detector is used by the UPC paths. The use of the pixel detector only, as opposed to using the whole tracker including the silicon strip detector, allows for quick track reconstruction saving computing cycles. The requirement of at least on reconstructed pixel track for the HLT triggers was designed to reject backgrounds where no particles are reconstructed by the tracker.

The total HLT output for the UPC trigger paths was 20 Hz. The limiting factor for the HLT rate was the amount of disk space available to store the data.

| HLT Trigger | |
|---|---|
| HLT_HIUPCNeuMuPixel_SingleTrack | Physics |
| HLT_HIUPCNeuEG2Pixel_SingleTrack | Physics |
| HLT_HIUPCNeuEG5Pixel_SingleTrack | Physics |
| HLT_HIMinBiasZDC_Calo_PlusOrMinus_v1 | Monitor |
| HLT_HIMinBiasZDC_PlusOrMinusPixel_SingleTrack_v1 | Monitor |
| HLT_HIUPCNeuHcalHfMuPixel_SingleTrack | Backup |
| HLT_HIUPCNeuHcalHfEG2Pixel_SingleTrack | Backup |
| HLT_HIUPCNeuHcalHfEG5Pixel_SingleTrack | Backup |

Table 4.2: List of 2011 HLT trigger.

## 4.3 Data Sets and Event Selection

### 4.3.1 Data Set

In order to investigate novel physics processes like UPC $J/\psi$ production, the LHC has delivered unprecedented amounts of data. The data for this analysis was recorded during the 2011 LHC PbPb run. During this period, 150 $\mu b^{-1}$ where recorded by the CMS detector, corresponding to over a billion PbPb collisions. Of this, 143 $\mu b^{-1}$ are used in this analysis.

Three specially selected samples were used for the present analysis (see Table 4.3). These samples were recorded using subsets of the triggers found in Section 4.2. The $J/\psi$ events discussed in this thesis were obtained analyzing the sample labeled in Table 4.3 as physics. A minimum bias sample was recorded for the sake of estimating efficiencies. Last, a zero bias sample was recored for investigating the ZDC and the noise distributions of HF. By recording this hierarchy of samples, interesting events are selected with a much higher purity in the physics sample, while the zero bias and minimum bias samples allow for the investigation of the selection criteria.

To record the physics sample containing the $J/\psi$ signal, a muon trigger was paired with a veto on energy in the BSC and a requirement that there be energy in at least one of two sides the ZDC. This trigger utilizes the unlikely chance of having overlapping noise in in the ZDC and muon detector. Because of the characteristically low momentum of UPC $J/\psi$ as compared to $J/\psi$ created by other physics process, the loosest muon trigger was used. The trigger rejects muon

| Sample | Events | $L_{int}$ |
|---|---|---|
| Physics | 300K | 143.3 $\mu b$ |
| Minimum Bias | 100K | X |
| Zero Bias | 5M | 580 b |

Table 4.3: Integrated luminosities and number of events for the three samples used in this analysis.

noise by requiring that a interaction took place that deposits energy in the ZDC. Contributions from hadronic interactions are reduced by the veto on the BSC. In this way the balance between reducing the rate and maximizing the efficiency was struck, allowing for the data to be recorded without producing high rates resulting in dead time for the detector.

In order to investigate the muon trigger and the other parts of the events selection, a minimum bias sample was recorded using the ZDC. For ZDC triggered sample, any event which had energy consistent with at least one neutron in either of the two sides of the ZDC was recorded. This process is much more common than the UPC $J/\psi$ production. For this reason, the rates of this trigger are much higher than the physics trigger, and only a small sub set of these events are recorded. From this trigger the pixel track efficiency was estimated.

In addition to the minimum bias and physics sample, a zero bias sample was recorded to examine the ZDC trigger and the HF noise distributions. The zero bias trigger fired every time both beams passed through CMS. Only 4 events out of every million triggered were recorded for this sample. This sample allowed for an unbiased measurement of the ZDC trigger efficiency as discussed in Section 4.6. Because the zero bias trigger does not require any activity in any of the CMS sub detectors, the sample contains very few hadronic collisions. This allowed for a measurement of the electronic noise distributions in the HF, which will be discussed in the next section.

The integrated luminosity for each of the three samples is calculated by recording activity in HF. The cross section for HF activity is measured from a van der Meer scan, and the cross section was found to be X. In this way the amount of integrated luminosity for any period running is related to the activity in HF. An additional method was used to cross check the integrated luminosity obtained by the van der Meer scan technique. The integrated luminosity can also be measured by counting the events that fire the L1 minimum bias trigger together with the inelastic PbPb cross

| cut | cut type | events |
|---|---|---|
| all triggered | – | 346841 |
| good vertex requirement | beam background rejection | 340997 |
| beam halo muon rejection | beam background rejection | 302777 |
| cluster shape compatibility requirement | beam background rejection | 233590 |
| single-sided neutron requirement | hadronic interaction rejection | 149992 |
| two track requirement | hadronic interaction rejection | 32732 |
| HF signal rejection | hadronic interaction rejection | 5392 |
| muon quality requirement | fake muon rejection | 1956 |
| J/$\psi$ mass requirement | kinematic cut | 662 |
| muon detectability cuts | kinematic cut | 541 |

Table 4.4: Effects of event selection cuts.

section.

## 4.3.2 Event selection

The analysis described in this thesis focuses on UPC $J/\psi$s decaying to muons. The trigger used for this analysis recored 346841 events. A set of off-line cuts were applied to increase the relative contribution of UPC events relative to background processes. The following cuts were applied.

Two sets of event selection cuts were applied to reject background events. The first set rejects background from the beam. The second rejects events where hadronic collisions have occurred.

To reject beam induced background the following cuts were applied:

- The reconstructed vertex must be within X cm in the transverse direction and X cm in the longitudinal direction. This cut insures that reconstructed particles come from interactions between the two beams rather than event where one of the two beams interact with gas particles near the interaction point.

- Beam halo muons were rejected using the timing of the muon hits. The beam halo cut rejects events where muons surrounding the beam stream through the detector.

- Pixel cluster shape should be compatible with the vertex. This cut requires that energy deposits in the silicon tracker point back to the reconstructed primary vertex.

These beam background cuts do not reject any UPC J/$\psi$ candidates.

The second set of background rejection cuts were designed to reduce contamination from hadronic interactions.

- No more than 2 reconstructed tracks in the event. The track requirement rejects events that produce many charged particles.

- Maximum reconstructed hit energy in HF was required to be below the threshold for electronic noise. Nearly all hadronic interactions ($\sim 98\%$) produce particles in the range $3 < |\eta| < 5$ covered by the HF detector. By requiring that the energy deposits in HF resemble noise, nearly all elastic hadronic collisions are expected to be rejected.

- Energy in the ZDCs consistent with neutrons on only one side of the interaction point. In hadronic interactions both nuclei break-up. By requiring that ZDC only reconstruct neutrons on one side of the interaction point, hadronic interactions that produce neutrons on both sides were rejected.

Each of these cuts are designed to reject topologies produced by hadronic interactions. The effect of these cuts can be seen in TableX.

To establish the HF noise thresholds, the noise distributions were measured in zero bias events. Only presences of both beams was required for these events to be recorded. An Off-line selection of events with no reconstructed tracks was used to insure that no collision had taken place. The HF noise threshold was defined as the cut that keeps %99 of the zero bias events. The noise distribution from this zero bias sample is compared to the physics sample and MC in Fig. 4.2.

The following standard muon quality cuts are applied:

- Tracker track matched with at least one muon segment (in any station) in both X and Y coordinates ($< 3 \sigma$).

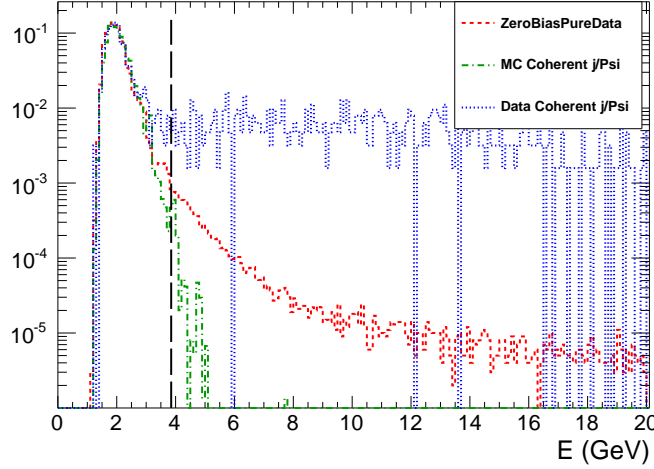- Cut on number of tracker layers with hits $> 5$.

- Number of pixel layers $> 0$.

Figure 4.2: Comparison of HF noise distributions in zero bias data, physics triggered data, and MC.

- The $\chi^2$ per degrees of freedom of the track fit $< 3$.

- Loose transverse and longitudinal impact parameter cuts, with in 3 cm in the transverse direction and withing 30 cm in the longitudinal direction with respect to the primary vertex.

These cuts are applied to reduce the number of fake muons.

## 4.4 Break up determination

As described in Section. 2.6, UPC J/$\psi$ photoproduction can be accompanied by the emission of neutrons from either of the two colliding nuclei. The various neutron emission scenarios, or break-up break up modes, can be distinguished by the ZDC. By separating events where the ZDC signal is consistent with 1 neutron versus several neutrons, the different break-up modes can be separated and compared to theory. For this reason, reconstruction of the ZDC signal plays an important role in this thesis. In order to maximize the ability to explore the one neutron peak, which sits at the bottom of the ZDCs dynamic range, a new ZDC reconstruction method was devised. This new reconstruction method was than used to establish a one neutron and many neutron threshold. In this section the ZDC signal reconstruction is described and how the neutron thresholds on this

signal were set.

### 4.4.1   ZDC Signal Reconstruction

The ZDC signal is built up from the pulse shapes for each of the 18 individual ZDC channels. The pulse shape is recorded in 250 ns second chunks and is divided into 10 time slices of 25 ns (See Fig 4.3). Counting from 0, the 4th time slice is synced with the timing of the rest of the detector and corresponds to when the products of the recorded collision reached the ZDC. For this reason the channel signal is taken from the 4th time slice.
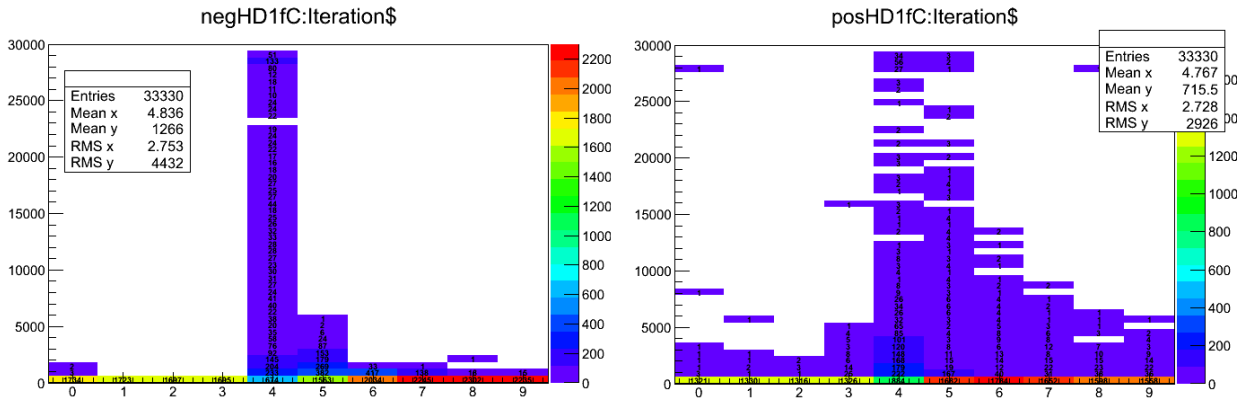


Figure 4.3: ZDC pluse shape.

The ZDC signal sits on top of a low frequency noise pedestal. Over the time scale of 250 ns, this low frequency noise signal appears as a constant that shifts randomly from event to event. The contribution from this noise is therefore measured event by event in order to subtract it. Time slice 5 is used for this purpose.

Time slices 1 and 2 could also be used to estimate the low frequency noise. However because the noise fluctuates to negative values of charge that can't be measured by the QIE, these time slice can only provide a measurement half the time. By using time slice 5 which contains the falling tail of the signal, the noise can be measured any time the signal raises significantly above the noise. If the fraction of signal in time slice 4 and 5 are constant and the noise contributes the same value to

both time slices, the following formula is applicable:

$$Ts4 \propto (Ts4 + C) - (Ts5 + C) = Ts4 - R_{Ts5/Ts4} * Ts4 = Ts4(1 - R_{Ts5/Ts4}), \qquad (4.1)$$

where $Ts4$ is the signal contribution in time slice 4, $Ts5$ is the signal contribution to time slice 5, $C$ is a random noise constant from the low frequency noise, and $R_{Ts5/Ts4}$ is the ratio between the signal contribution from time slice 5 over time slice 4. Fig. 4.4 demonstrates the consistence of the fraction and validates the unconventional method of using the falling tail of the signal to estimate the low frequency noise. By using time slice 5 the chances measuring the noise are maximized allowing for the possiblity to sperate the signal from the noise and measure the ZDC signal near noise at the bottom of the ZDC dynamic range.
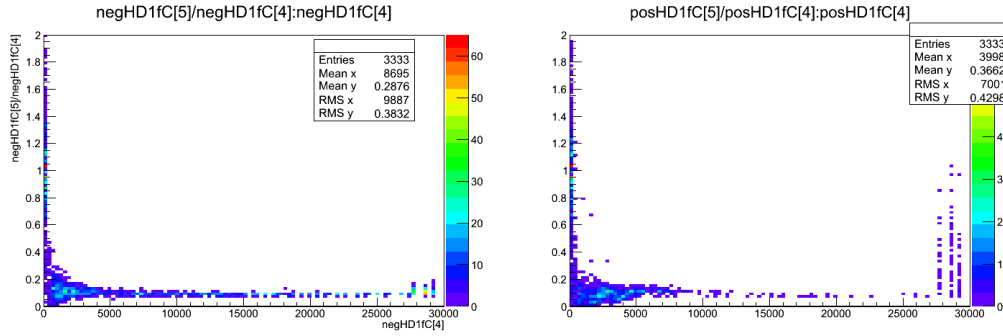


Figure 4.4: The fraction of signal in time slice 5 over time slice 4 as a function of the signal in time slice 5 in ZDC$^-$ (left) and ZDC$^+$ (right).

To measure one signal value for ZDC$^+$ and one for ZDC$^-$, the signals from each of the channels are combined. Channels from the EM section and HD section are combined first. Only channels with signal above zero in time slice 5 and time slice 4 are included. The EM section of the calorimeter is more densely packed with optical fibers and therefore has a higher gain relative to the HAD section. To account for this, the combination of EM channels is weighted with a factor of 0.1 to match the HAD channel gains. The value for each side of the ZDC's signal is given by the sum of the HAD channel combination and weighted EM channel combination. It is this signal, one for ZDC$^+$ and one for ZDC$^-$, which is plotted to measure the neutron thresholds.

## 4.4.2 Determination of the one neutron thresholds

The ZDC thresholds used to establish the various break-up modes were measured from zero bias data. By using this dataset, the spectrum does not contain a trigger bias. The trigger requirement for the zero bias events is that both beams were present in CMS. This does however include a significant electronic noise contribution due to events where no neutrons are emitted in the direction of the ZDC.

To determine the thresholds for one and multiple neutrons, the $ZDC^+$ and $ZDC^-$ spectra are fit. Four Gaussian functions were combined to fit the spectra. The electronic noise was fit to a Gaussian about zero. The one, two, and three neutron peaks are fit to Gaussians that are successively broader. The mean of each peak was initially set to multiples of the mean of the one neutron peak. The
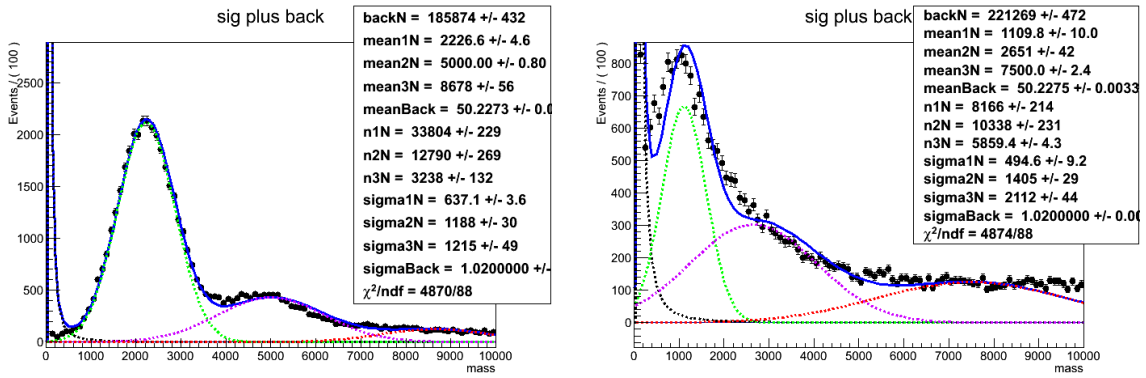


Figure 4.5: Fit to the signal spectra for $ZDC^-$ (left) and $ZDC^+$ (right)

threshold for a neutron in the ZDC was taken from the fits in Fig. 4.5. Any signal greater 2 $\sigma$ below the mean of the one neutron peak was considered signal. Any signal greater than 2 $\sigma$ above was considered multiple neutrons. In this way the single neutron break up modes could be separated from the multiple neutron modes.

Several of the break-up mode calculations that have been done involve single sided configurations where neutrons are present on one side of the interaction point and not the other. To identify signal consistent with noise, noise distributions for the combined EM sections and the combined HAD sections were measured. The beams are only made to collide every 200 ns. In Fig. 4.3 higher than average signal can be seen in the 0th time slice, which precedes the main signal time slice time

slice 4 by 200 ns. This is due to events where activity was present in the ZDC for two consecutive collisions. Time slices 1 and 2, however, occurred between collisions. These time slices were used to estimate the noise spectrum.
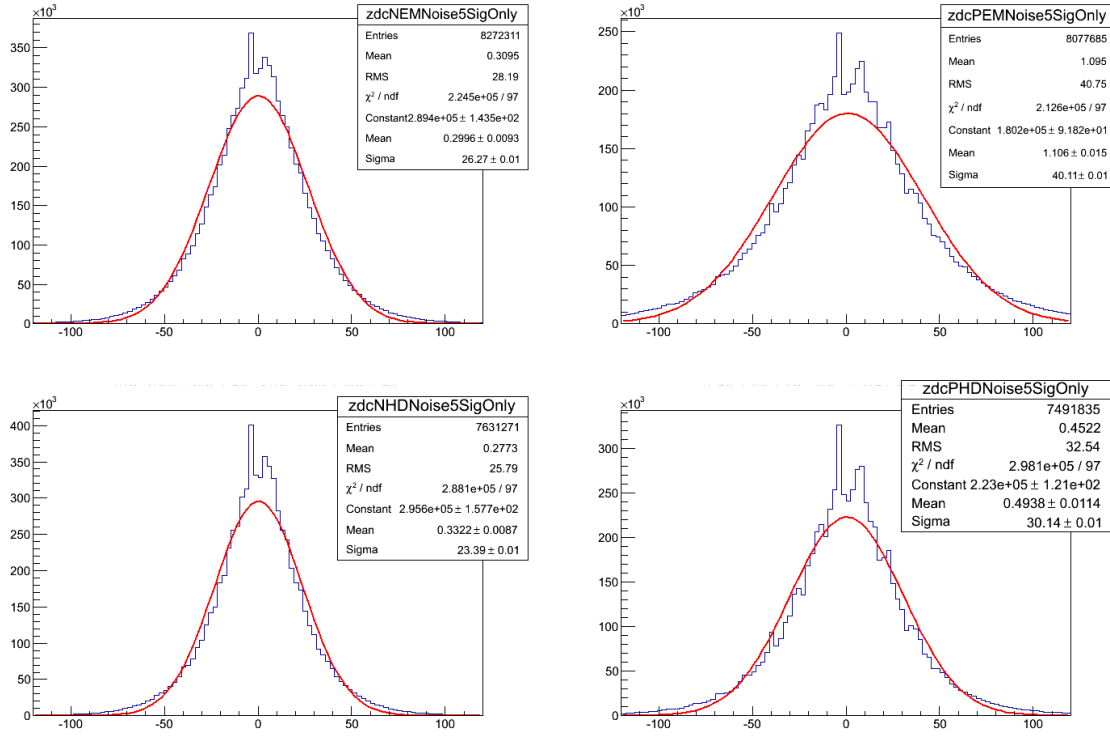


Figure 4.6: ZDC noise spectra from $ZDC^-$ EM section (upper left), $ZDC^+$ EM section (upper right), $ZDC^-$ HAD section (lower left), and $ZDC^+$ HAD section (lower right).

Fig 4.6 shows the noise spectrum for each of the EM and HAD sections for the two sides of the ZDC. As with the signal measurements, the low frequency noise pedestal is subtracted event by event by subtracting time slice 2 from time slice one before the channel signals are combined for each section. A side is considered consistent with noise if both HAD section and EM section signal measurements from the signal method involving time slice 4 and time slice 5 are lower than 2 sigma below the mean in Fig. 4.6. With the single nuetron, multi-neutron, and noise thresholds established, the contributions to the various break-up modes were estimated and compared to theory.

48

## 4.5 Signal extraction

After all event selection cuts, the coherent J/$\psi$, incoherent J/$\psi$, and photon-photon process all contribute to the remaining events. Each process must be separated from the final mix. To achieve this, the invariant mass and $p_T$ distributions are used to distinguish between the three processes. The photon-photon process is extended in invariant mass whereas the J/$\psi$ is peak strongly near 3.1 GeV. In $p_T$ the photon-photon and coherent process have similar distributions, both peaked shapely below 0.1 GeV, whereas the incoherent process is more broadly distributed across an interval extending to nearly 1 GeV. The mass distribution was fitted to separate the photon-photon process from the J/$\psi$ process. The $p_T$ distribution was used to separate the incoherent process from the photon-photon process, and the coherent process. In this way, a separate yield was extracted for all three processes.

The invariant mass distribution for opposite sign dimuons is shown in Fig. 4.7. A J/$\psi$ signal is clearly visible together with tails at higher and in lower mass due to the photon-photon process. A fit to the invariant mass distribution was done using a Gaussian to account for the J/$\psi$ signal and a first order polynomial function for the photon-photon process. The extracted number of J/$\psi$ candidates from this fit includes all J/$\psi$s in the mass window that passed the analysis cuts, i.e. both coherent and incoherent process contribute to yield from the mass fit. The $p_T$ distribution is needed to separate the two different contributions to the J/$\psi$ peak.

The same candidates from Fig. 4.7 are plotted as a function of $p_T$ in Fig. 4.8. The clear overlap of the coherent and photon-photon process, and the clear separation of these two lower $p_T$ processes from the incoherent process are apparent. The shape of the $p_T$ distribution for the coherent, incoherent, and photon-photon process are taken from the final output of MC after applying all analysis cuts. To obtain the yields for each of the three process, the $p_T$ distribution was fit to the three templates. In Fig.4.8, the yield parameters that were fit were left unconstrained for all three process.

The shape of the photon-photon process and coherent J/$\psi$ are very similar in $p_T$. Accordingly, the contribution from the photon-photon process and the coherent process are difficult to separate
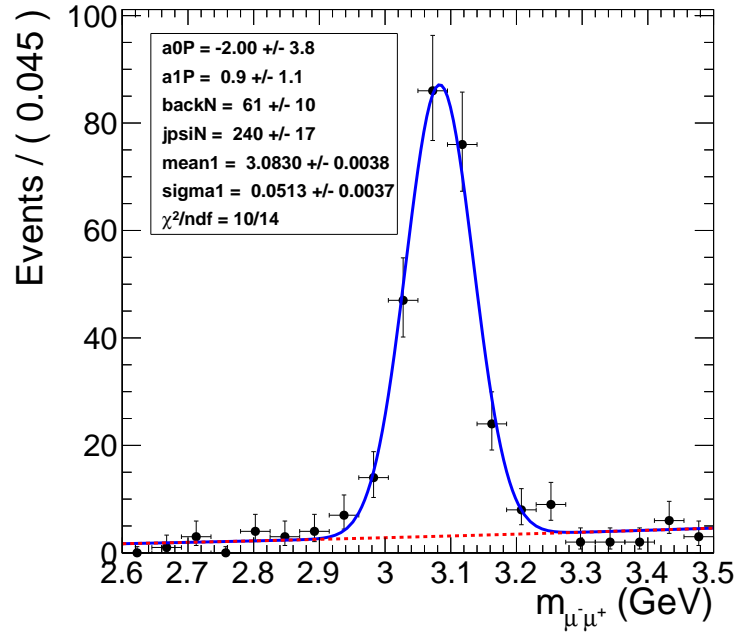
Figure 4.7: Mass fit to J/ψ using Gaussian for the signal and a first order polynomial for the photon-photon continuum
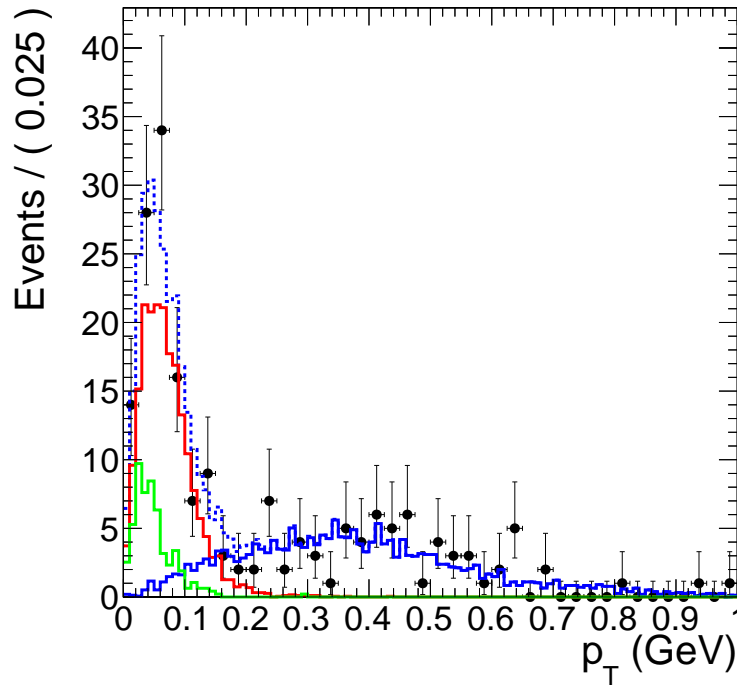


Figure 4.8: Fit to MC $p_T$ templates.

from the $p_T$ distribution. The confidence contours in Fig. 4.9 from the template fit in Fig. 4.8 demonstrate the strong anti-correlation between the coherent yield parameter, *nCo*, and the yield

parameter for the photon-photon process, *nGamma*. Because of the anti-correlation, the statistical uncertainty on *nCo* and *nGamma* from the fit are larger than $\sqrt{nCo}$ and $\sqrt{nGamma}$ expected from Poisson statistics. The information from the invariant mass and $p_T$ distributions was combined to break this correlation. Through this combination, the contribution to the final yield from the three process was measured.
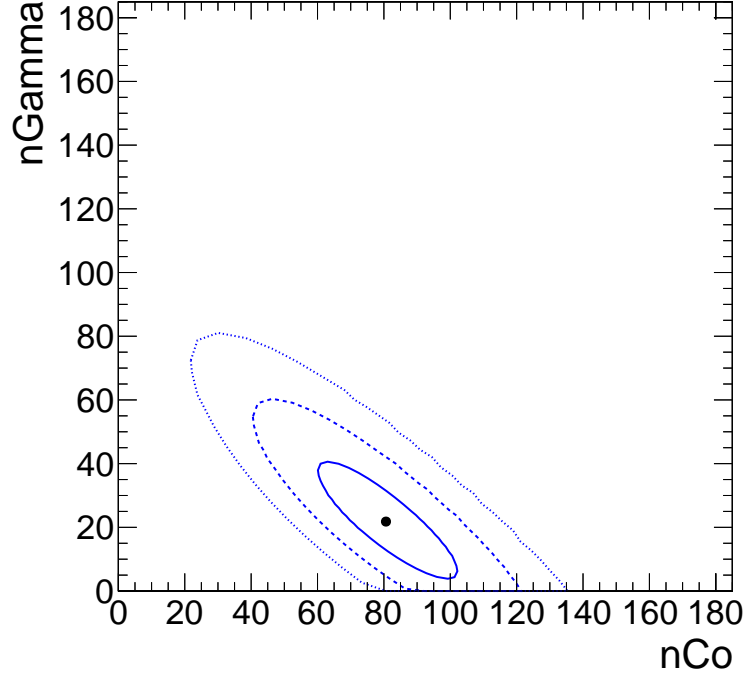


Figure 4.9: 68%, 95%, and 99% confidence contours from the $p_T$ template fit.

To utilize the mass fits ability to distinguish the photon-photon process from the coherent and incoherent process all while utilizing the $p_T$ fits ability to separate the coherent and photon-photon processes from the incoherent, a simultaneous fit to the mass spectrum and $p_T$ spectrum was preformed. Fig. 4.10 shows the result of the simultaneous fit. The simultaneous fit forces the parameter *nGamma* to both describe the photon-photon continuum present in the side bands of the J/$\psi$ mass peak as well the photon-photon contribution to the low-$p_T$ part of the $p_T$ spectrum. In addition, the J/$\psi$ yield from the mass fit is forced to equal the contribution from from the incoherent and coherent process in the fit to the $p_T$ distribution. In this way, the correlation between the yield parameters was broken, and the contribution from the three process are left independent of each
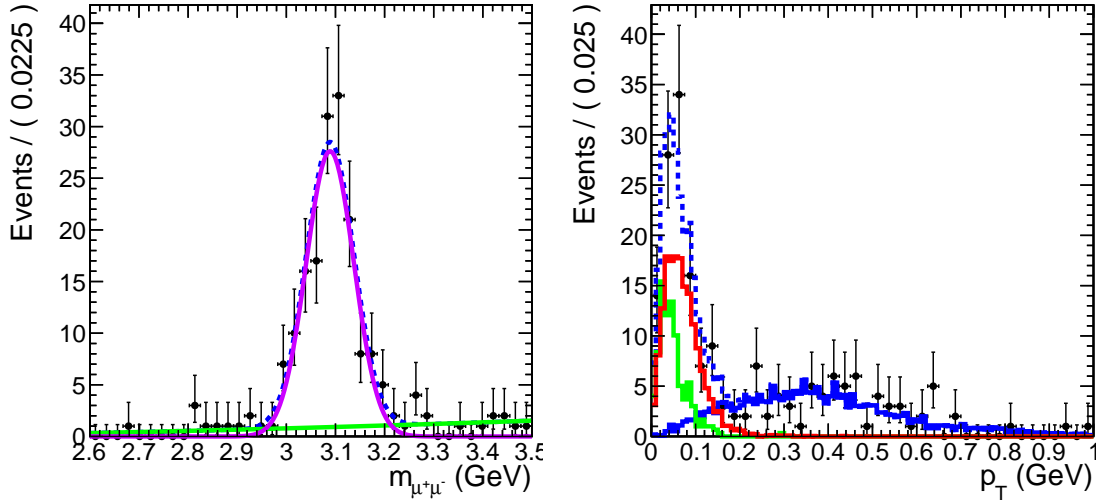
other.



Figure 4.10: Simultaneous fit to the mass and $p_T$ spectra.

By simultaneously fitting both the mass and $p_T$ spectra, the yields from the coherent, incoherent, and photon-photon process were separated from each other in total yield of final candidates. The ambiguity between the coherent and incoherent processes in the mass fit the ambiguity between the coherent and the photon-photon process was over come by combining the two fits. Fig. 4.11 shows the confidence contours for nCo and nGamma from the simultaneous fit in Fig. 4.10. The slope of the confidence contours in Fig. 4.11 is noticeably closer to 0 than the apparent negative slope in Fig. 4.9. The contours for the simultaneous fit are also reduced compared to Fig. 4.9 with widths in *nCo* and *nGamma* similar to those expected from Poison statistics. From the simultaneous fit, reasonable statistical errors were obtained along with the yields for the three processes.
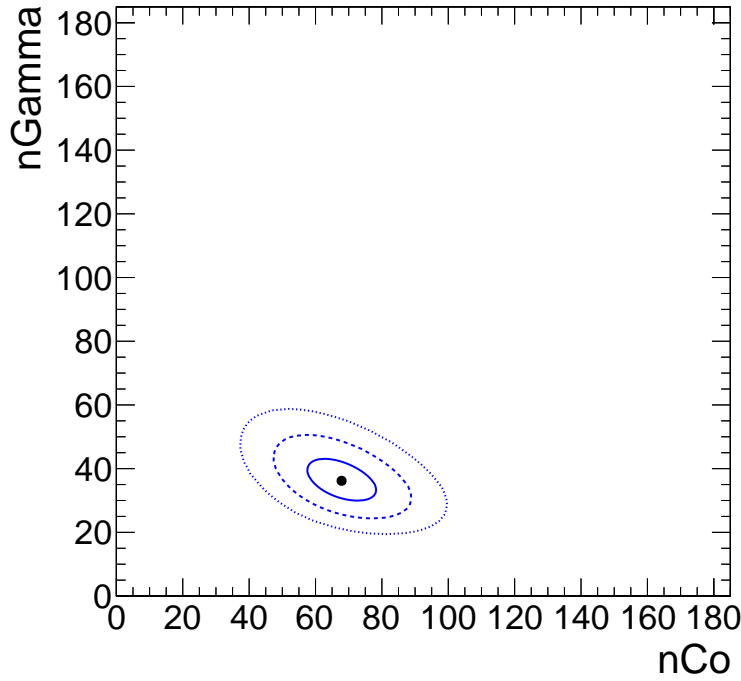
Figure 4.11: 68%, 95%, and 99% confidence contours from the simultaneous fit.

## 4.6 Efficiency determination

### 4.6.1 Muon Efficiencies

The muon efficiencies are measured from MC and data. The MC based measurement accounts for the detector acceptance and the efficiency of the muon quality discussed in Section 4.3. The trigger efficiencies were measured in data using the tag and probe method, which is discussed below.

CMS has a limited acceptance for $J/\psi$s, particularly in the case of $J/\psi$s with low momentum like those produced in UPC events. To measure the acceptance of CMS for $J/\psi$s, reconstructed dimuon candidates were considered detectable if both reconstructed daughters fell into a detectability region. This region was defined using the coherent $J/\psi$ events obtained from STARlight. The efficiency for reconstructing single muons $\varepsilon_{reco}^{\mu}$ is defined by $\varepsilon_{reco}^{\mu} = \frac{N_{reco}^{\mu}}{N_{gen}^{\mu}}$, where $N_{reco}^{\mu}$ is the number reconstructed muons after after the full CMS detector simulation and that pass the standard muon quality cuts, and $N_{gen}^{\mu}$ is the number of generated muons from STARlight. Fig. 4.12 shows the efficiency for reconstructing single muons from coherent $J/\psi$ events. To avoid the edges of the
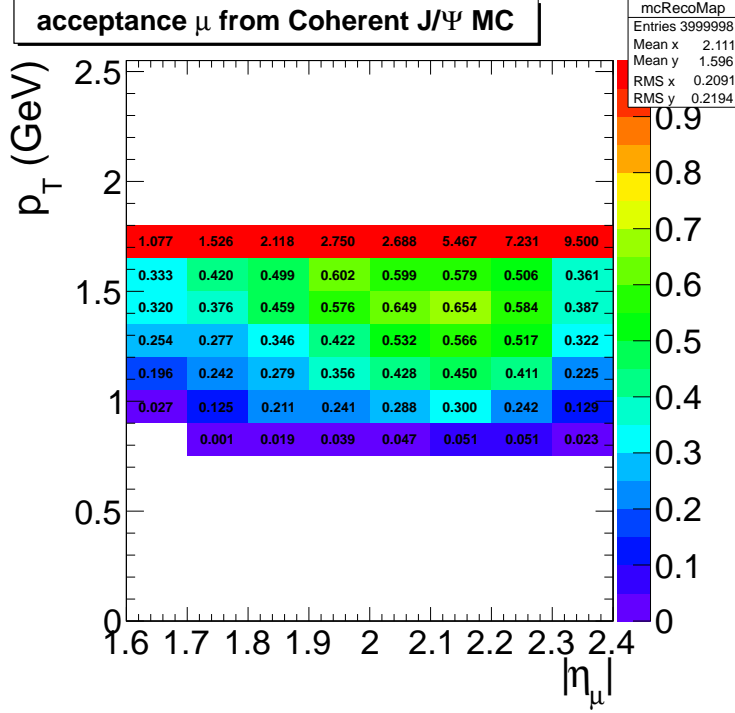
Figure 4.12: Muon daughter detectability from coherent J/$\psi$, incoherent J/$\psi$, photon-photon, and J/$\psi$ gun samples.

detectors acceptance, all reconstructed muons that fall into a $(p_T, |\eta|)$ bin that has an efficiency less than 20% were rejected thus defining the detectability region. The acceptance for reconstructing dimuons was calculated from MC using the following formula:

$$A = \frac{N_{det}(|y|, p_T)}{N_{gen}(|y|, p_T)},$$

(4.2)

where $N_{det}$ is the number of reconstructed dimuons where both daughters fall in to the detectability region, and $N_{gen}$ is the number of generated dimuons. From Eq. 4.2, the acceptance for $J/\psi$ was calculated as a function of $|y|$, and $p_T$ (see Fig. 4.13).

The tag and probe method is used to measure the trigger efficiency of the muon daughters, which is a data driven approach. In this method there are three categories of daughter muons. Tag muons are high quality muons. Passing probes are reconstructed muons that match the muon trigger, while failing probes do not. Each dimuon will have one daughter classified as a tag and the other as a probe. From here three invariant mass histograms are studied. One histogram is
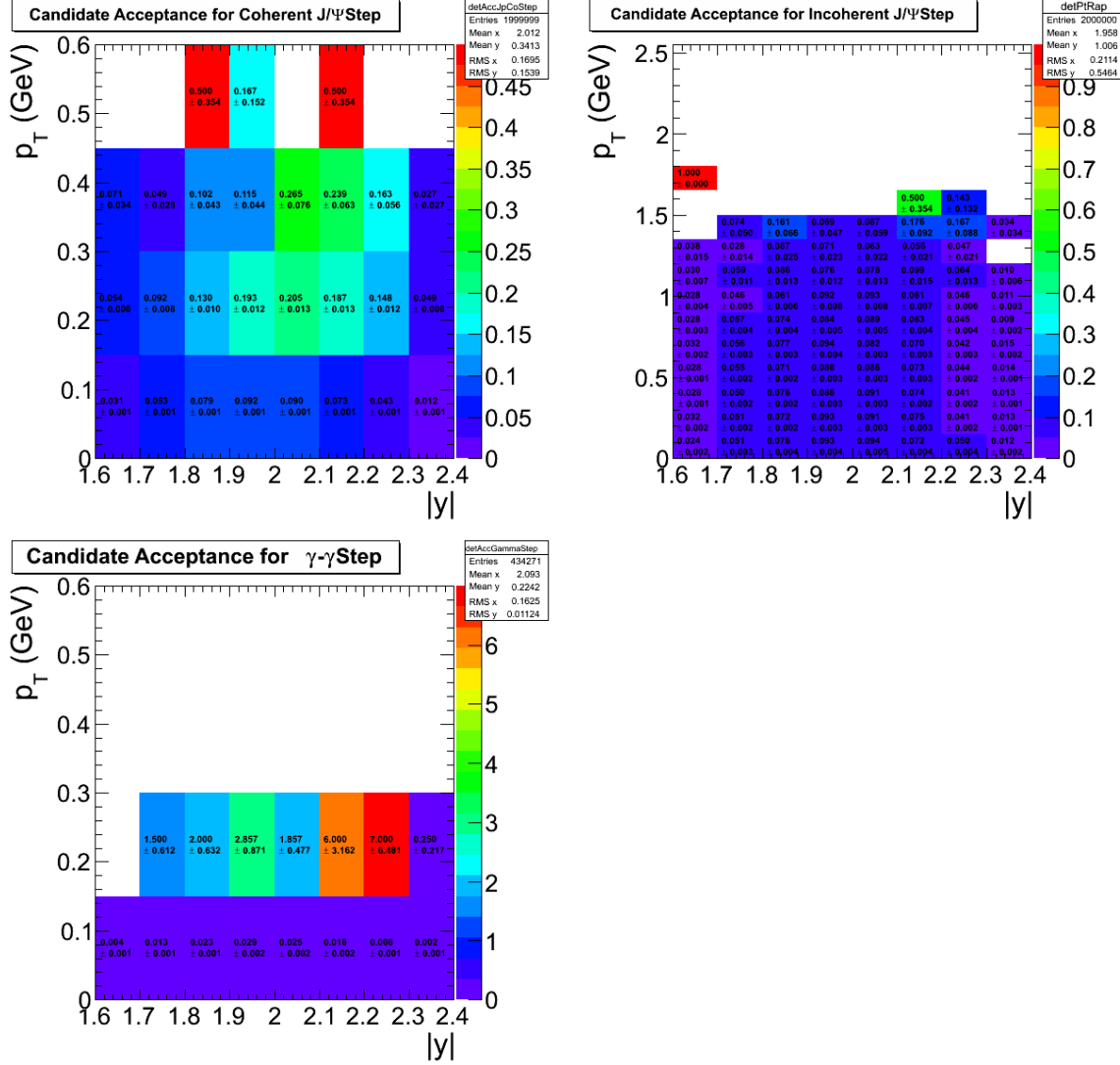
Figure 4.13: Dimuon acceptance from coherent J/$\psi$ (top left), incoherent J$\psi$ (top right), and photon-photon interactions (lower).

created from all pairs. The second comes from pairs where the probe is a passing probe. The last histogram comes from pairs where the probe fails to fulfill the trigger, *i.e.* the probe is a failing probe. Because this depends on the $p_T$ and $|\eta|$ of the probe, one set of three histograms for each $(p_T, |\eta|)$ bin of the probe is created.

To extract the single muon trigger efficiency $\varepsilon_{trig}^{\mu}$, each set of invariant mass histograms was simultaneously fitted. The signal was fitted using a Crystal Ball function, and the background was fitted to an exponential. The Crystal Ball parameters were simultaneously fitted to all three

histograms. The exponential function was fitted to the failing and passing probe histograms separately. Because the background shapes are in principal different for the two samples, the efficiency is driven by this difference.

To measure the trigger efficiency a tag is required to pass all muon quality cuts and matched to the trigger. The probe is required to pass all quality cuts. A passing probe is a probe that is also matched to the trigger. In this way the tag leaves the probe in biased by the trigger and the efficiency can be mesued by fitting mass.

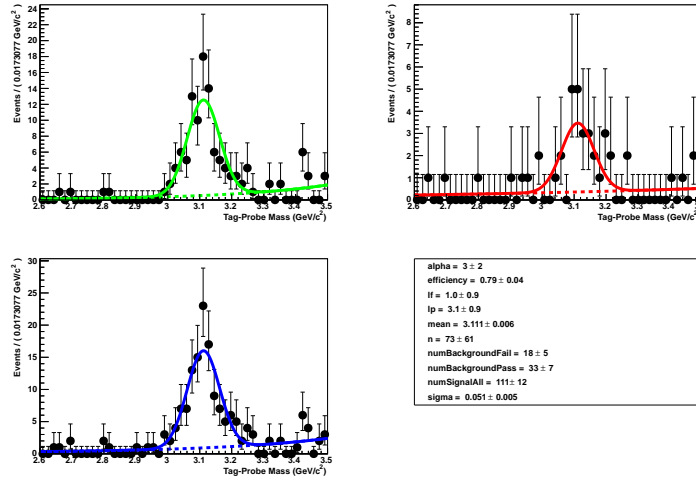Fig. 4.14 shows the fit of the three sets of pairs. This fit is done for each bin of the probes $p_T$



Figure 4.14: Fits to tag and probe pairs in the J/$\psi$ mass region.

and $\eta$. The resulting fit is in Fig. 4.15.

The dimuon trigger efficiency $\varepsilon_{dimuontrigger}$ was measured from the single muon efficiencies. The efficiency of each candidate was calculated using the following equation:

$$\varepsilon_{dimuontrigger} = 1 - (1 - \varepsilon_{trigger}^{\mu_1})(1 - \varepsilon_{trigger}^{\mu_2}), \tag{4.3}$$

where $\varepsilon_{trigger}^{\mu_1}$ is the tag and probe efficiency of the first dimuon daughter, and $\varepsilon_{trigger}^{\mu_2}$ is the efficiency of the second muon daughter. In Eq. 4.3 the probability of at least one daughter firing the trigger is calculated by subtracting one from the probability that neither daughter fires the trigger, thus giving the dimuon trigger efficiency.
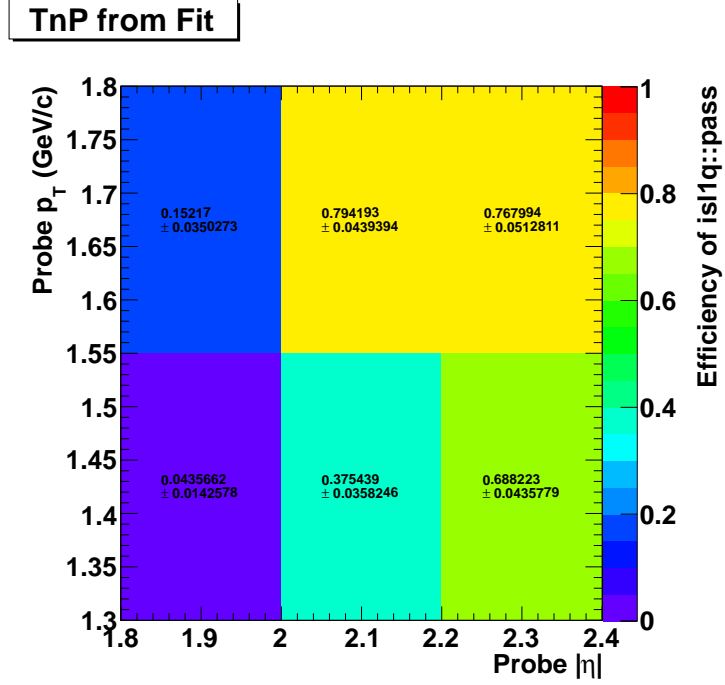
56

Figure 4.15: Muon trigger efficiencies in $p_T$ and $\eta$ bins from the tag and probe method.

The average dimuon trigger efficiency for each dimuon $(p_T, |y|)$ bin was calculated by averaging the individual dimuon candidates in each bin. The average trigger efficiency was multiplied by the acceptance from the MC to produce a total efficiency times acceptance factor.

## 4.6.2 ZDC trigger efficiency

A special trigger was prepared to monitor the ZDC trigger efficiency. This trigger required either a $ZDC^+$ or $ZDC^-$ trigger, together with at least one pixel track. Events were accepted offline if there was no activity in the BSCs or activity on a single side. This sample suffers from a trigger bias. For example, a sample triggered by $ZDC^+$ would always produce a $ZDC^+$ trigger efficiency of one. To avoid this, the special trigger sample was divided into two subsamples in the following way. A first sample triggered by the $ZDC^+$ input and second one triggered by the $ZDC^-$. The $ZDC^+$ trigger efficiency is measured from the $ZDC^-$ sample, and vice versa.

The trigger efficiency for reconstructed ZDC energies above the single neutron threshold were estimated (see for Sec. 4.4). The $ZDC^+$ efficiency was calculated using the $ZDC^-$ triggered sam-
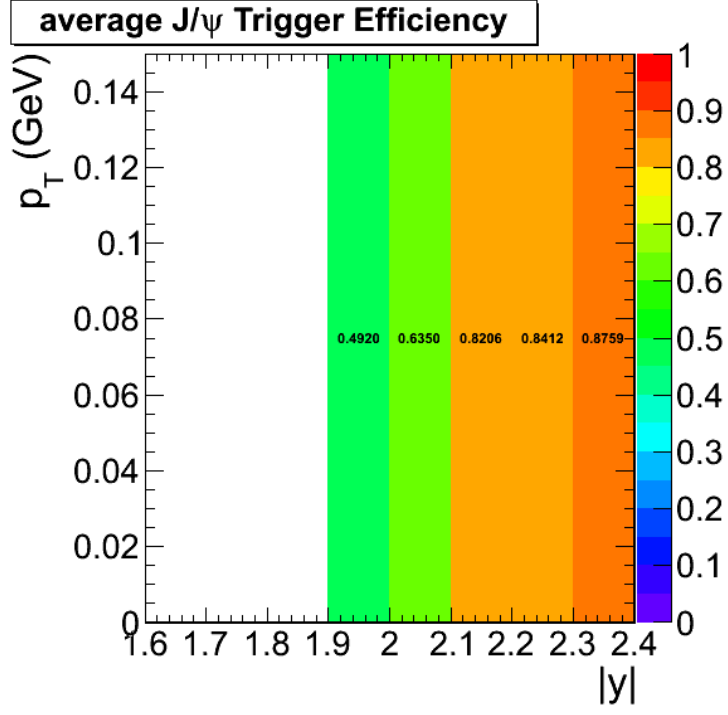
Figure 4.16: The trigger efficiency from tag and probe averaged over candidates in each $(p_T, |y|)$ bin.
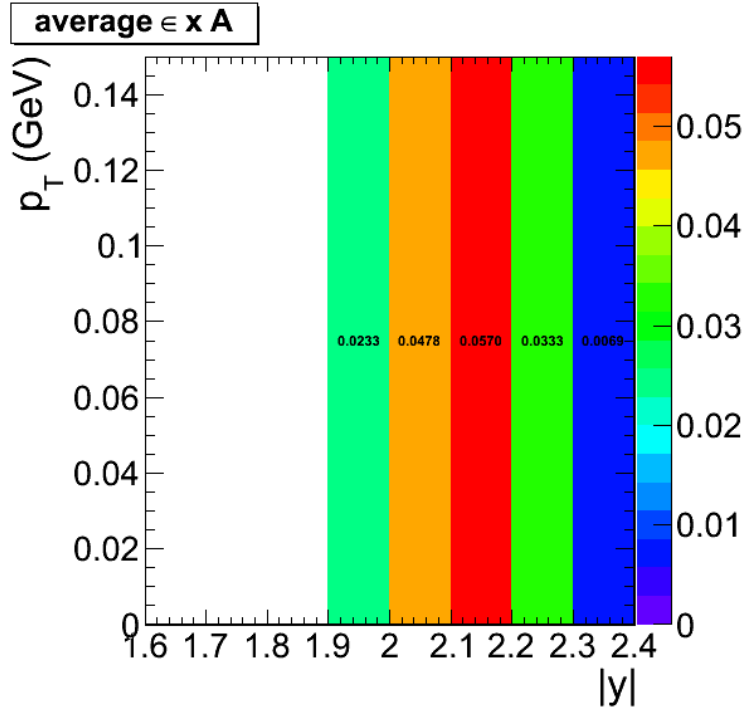


Figure 4.17: The acceptance times averaged trigger efficiency from tag and probe.

| ZDC Side | Reco Method | $N_{events}$ | $N_{trig}$ | $\varepsilon_{ZDC}$ |
|:---:|:---:|:---:|:---:|:---:|
| $ZDC^+$ | 1 | 72946 | 71688 | $0.982 \pm 0.005$ |
| $ZDC^+$ | 2 | 73028 | 71706 | $0.9819 \pm 0.005$ |
| $ZDC^-$ | 1 | 76137 | 71786 | $0.9429 \pm 0.005$ |
| $ZDC^-$ | 2 | 76132 | 71859 | $0.9439 \pm 0.005$ |

Table 4.5: ZDC trigger efficiencies for ZDC reconstruction method 1 and 2

ple. To estimate the efficiency, the number of events with energy in $ZDC^+$ greater than the single neutron threshold, $N_{events}$, were measured. From this set of events, the number of events that also fire the $ZDC^+$ are measured. The ratio between the number of single neutron events that fire the trigger and all single neutron events was taken as the estimate of trigger efficiency. The same procedure is applied for each side of the ZDC.

## 4.7 Systematic checks

### 4.7.1 HF noise threshold

The way in which the HF noise distribution is measured effects the event selection. In addition, this cut plays a significant role in rejecting hadronic events. In Table 4.4 the importance of cutting on HF noise is evident. The HF noise cut rejects X of the events the remaining. The systematic uncertainties on the HF noise requirement is important for this reason. The result must not depend significantly on the method used to apply the cut on the noise because of the large reduction of events that result from it.

Four different approaches were employed to estimate the systematic effect arising from picking a particular method. By looking at the variation of the number of events that remain after applying the thresholds derived from these four methods, the systematic uncertainty for the HF noise cut was estimated. The four methods are derive from combinations of two variations. The type of object was varied from a low-level detector object called a RecHit to a higher level physics object called a CaloTower. The distinction between the two is that the RecHit is the energy deposited in a single calorimeter detector element, where as the CaloTower is a collection of RecHits with varrious

thresholds, which represent a full energy deposit that would come from a particle or a collection of particles from a jet passing through the detector. The second variation is on the separation of the two sides. In one case the threshold is derived for the two sides combined. In another case the thresholds are calculated separately for the two sides of HF. By combining these two variations a total of four estimates of the effect of the HF noise cut were made. Table 4.6 below shows the thresholds that are measured for each of the four methods. The resulting yields from the four different methods are displayed in Table 4.7.

| Object type | HF (GeV) | $HF^-$ (GeV) | $HF^+$ (GeV) |
|---|---|---|---|
| RecHits | 3.85 | 3.25 | 3.45 |
| CaloTowers | 4.25 | 3.25 | 3.75 |

Table 4.6: HF noise theresholds for various noise measurement methods.

| Object type | Combinded HF threshold | Two-sided thresholds |
|---|---|---|
| RecHits | 298 | 290 |
| CaloTowers | 302 | 288 |

Table 4.7: Candidate yields below 1.05 GeV $p_T$ for various HF noise cuts.

The threshold was adjusted to estimate the effect of tightening the requirement on the zero bias data. By successively lowering the percentage of the zero bias sample that was included, the HF noise cut was made more restrictive including first 98%, than 97% of all zero bias events. This was done for both object types, RecHits and CaloTowers. This allows for an estimate of the systematic uncertainty on selecting a 99% cut. Table 4.8 shows the effect on the thresholds themselves for both RecHits and CaloToweres, whereas Table 4.9 shows the effect on the candidate yields.

Table 4.8: Values of the energy cuts for the HF calorimeter for RecHit and CaloTower in GeV.

| % | $E_{RecHit}$ GeV | $E_{CaloTower}$ GeV |
|---|---|---|
| 99 | 3.85 | 4.25 |
| 98 | 3.25 | 3.75 |
| 97 | 2.95 | 3.25 |

Table 4.9: Number of dimuon candidates with $p_T$ <1.05 when changing HF calorimeter cuts for RecHit and CaloTower.

| % | RecHit cut | CaloTower cut |
|---|---|---|
| 99 | 298 | 302 |
| 98 | 287 | 294 |
| 97 | 284 | 280 |

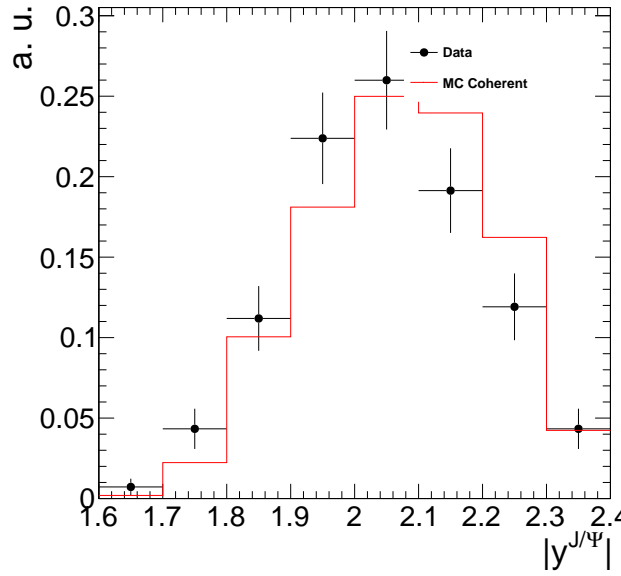### 4.7.2 MC vs Data compairson



Figure 4.18: Comparison of the of the dimuon rapidity distributions between coherent MC sample and Data.

### 4.7.3 Tag and probe

To estimate the effect the tag and probe fits, the tag and probe efficiencies were additionally measured by counting probes in the J/$\psi$ mass window.

### 4.7.4 Template fit

The normalization for the coherent and incoherent templates are left free. To address this issue the template from the photon-photon process was fixed to the cross section value given by STARlight
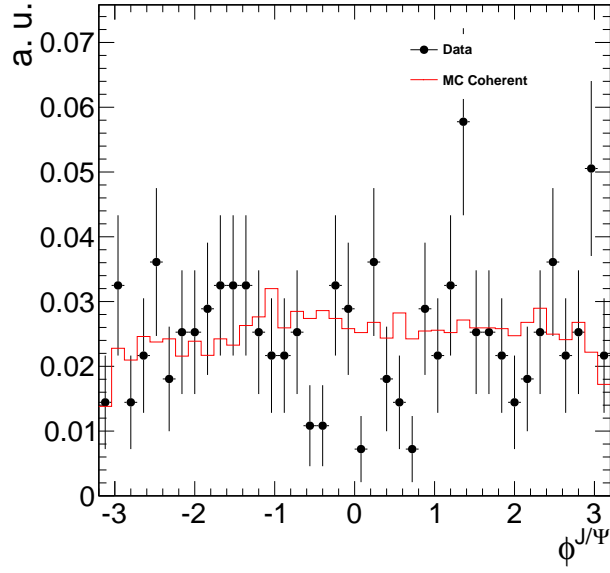
Figure 4.19: Comparison of the of the dimuon $\varphi$ distributions between coherent MC sample and Data.

and normalized to the integrated luminosity of the data. The normalization for the photon-photon template was allowed a range of 20% due to the 20% uncertainty in the STARlight cross section.

The systematic uncertainty for the contribution to the three components of the signal was estimated by varying the mass fit. Because the mass fit is used to fix the contribution to the $p_T$ spectrum of the photon-photon process, the change of the mass fit results in different coherent contributions from the $p_T$ template fit.

Moving from left to right in Fig 4.23 the contribution from the photon process increases. The left most fit uses a Crystal Ball function to account for the radiative decay of the final state daughters of the J/$\psi$. The low mass exponential portion however picks up background events and over-estimates the J/$\psi$ contribution. The right most plot fits the background to a 2nd order Cheby-Chev polyinomial, which overestimates the background. Because the Cheby-Chev peaks just below the J/$\psi$ peak, this fit overestimates the background and in turn underestimates the signal contribution. The Gaussian fit with a linear background however does a reasonable job of fitting both the background and the signal.

From these three fits an upper and lower bound of the systematics due the choice of fit functions
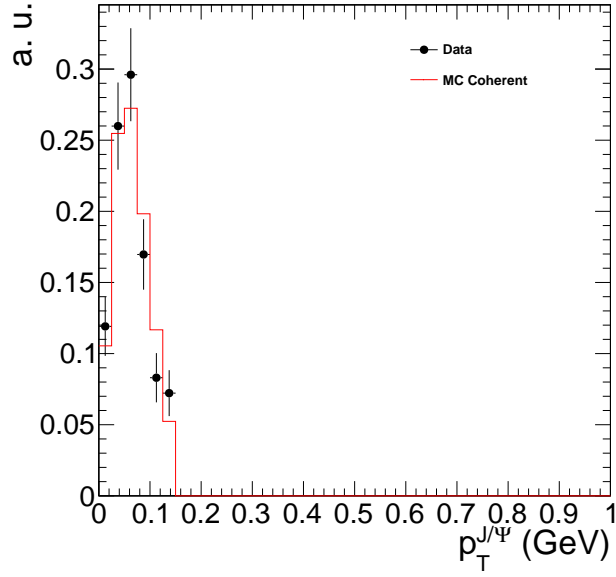
Figure 4.20: Comparison of the of the dimuon $p_T$ distributions between coherent MC sample and Data.
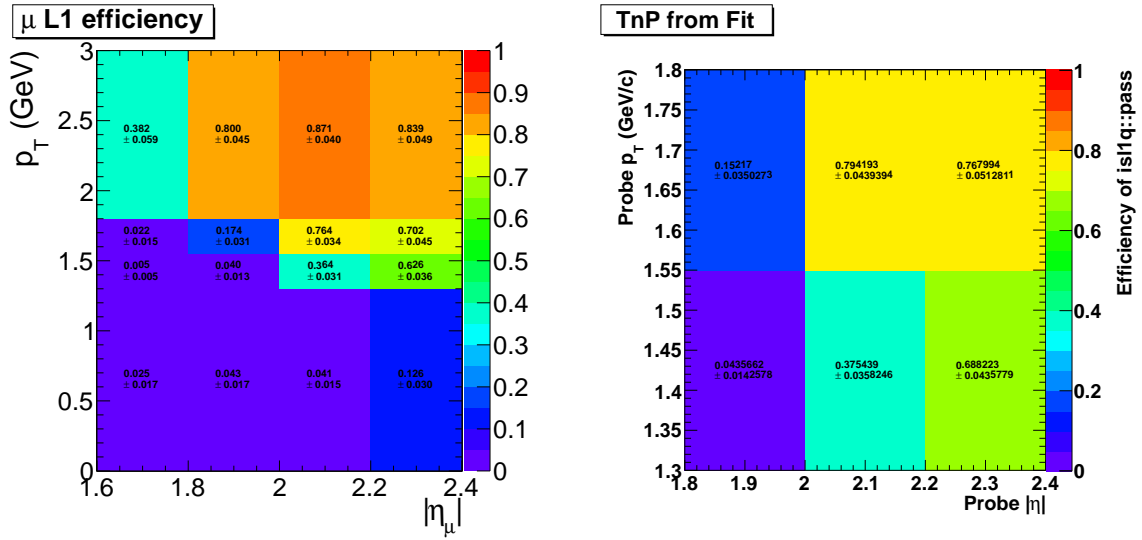


Figure 4.21: Tag and probe trigger efficiencies from counting (left) compared to fitting (right)

was estimated.

## 4.7.5 Mass fit

Fig. 4.24 demonstrates the small dependence the raw J/$\psi$ yield has on the fitting function. Both fit functions agree well, with reduced $\chi^2$ values below one. The Crystal ball fit give an upper estimate
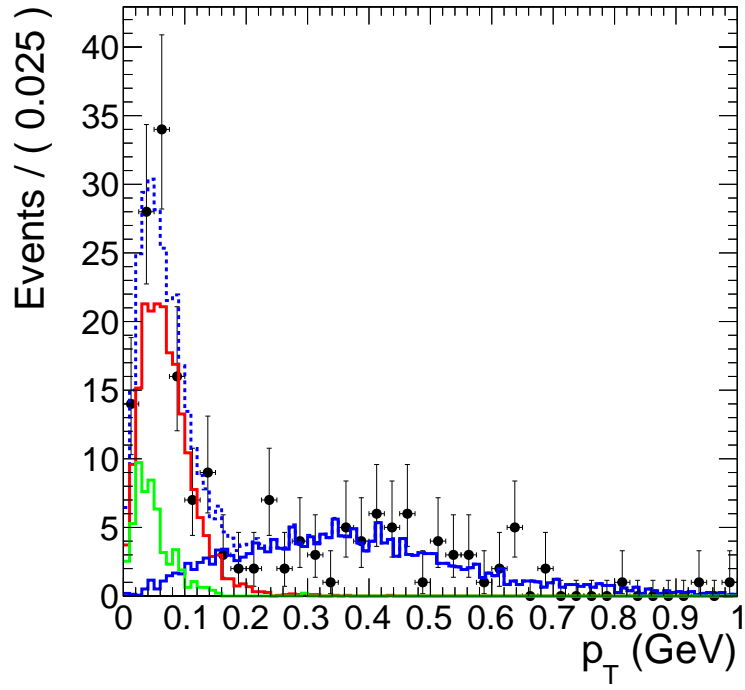
63

Figure 4.22: Coherent, incohernt, and photon-photon process $p_T$ template fit to data.
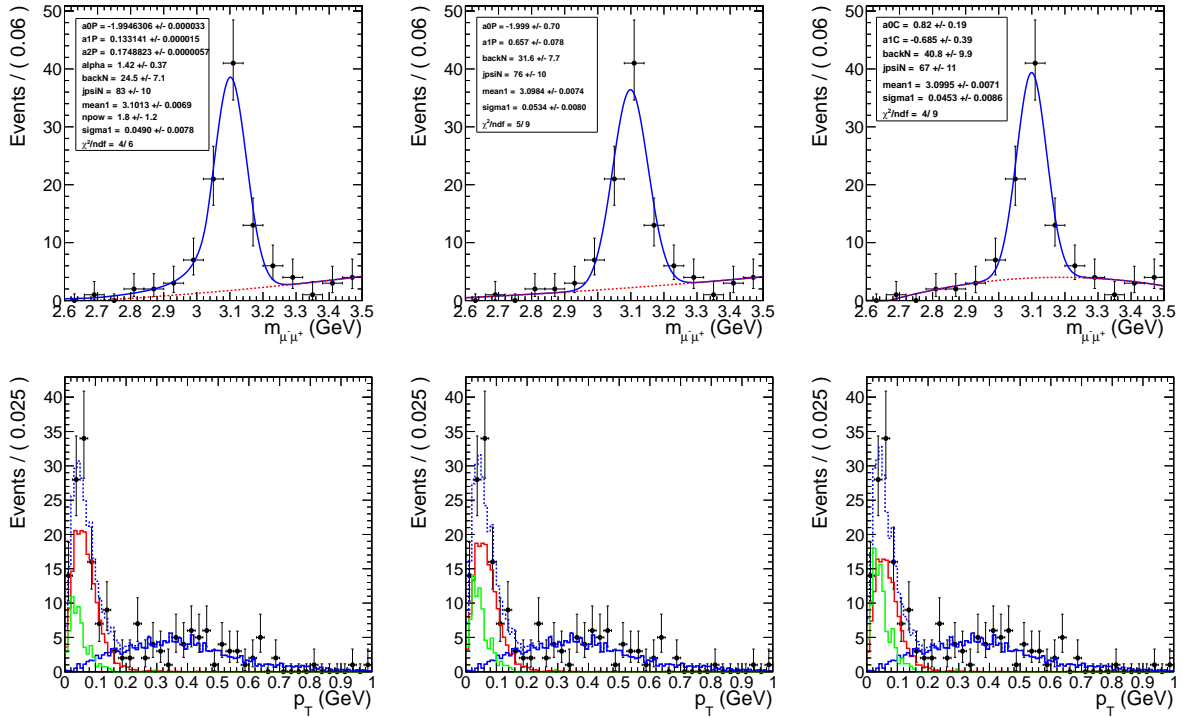


Figure 4.23: Various mass distribution fits and the corresponding $p_T$ template fit.

64
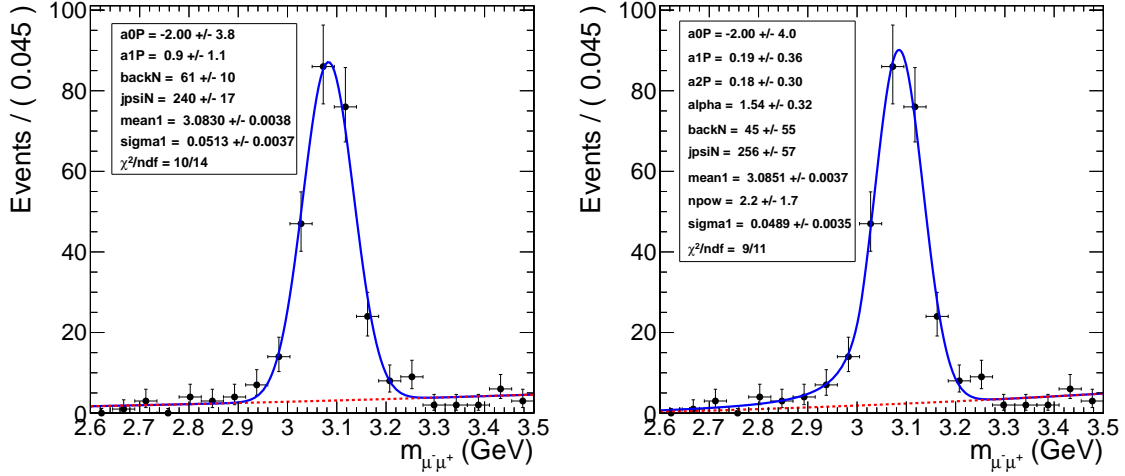
Figure 4.24: Mass fit to J/$\psi$ using Gaussian (Left) and Crystal Ball (Right) for the signal and a polynomial for the background

for the J/$\psi$ yield. The Gaussian fit gives an lower estimate. The main difference comes from the lower mass tails. In the Crystal ball fit the lower tail is considered to be signal due to shifting of the mass spectrum to lower mass due to radiation from the final state muons. In the Gaussian fit the lower mass tail is considered to be background and the signal is sharper.

As check on the simultaneous $p_T$ and mass fit, the mass fit is done using mass templates from STARlight.



Figure 4.25: Simultaneous fit to the mass and $p_T$ using mass templates for the mass fit.

### 4.7.6 MC acceptance

To estimate the effect of the GEN level $p_T$ distribution on the acceptance the incoherent sample was used to correct the coherent yield.
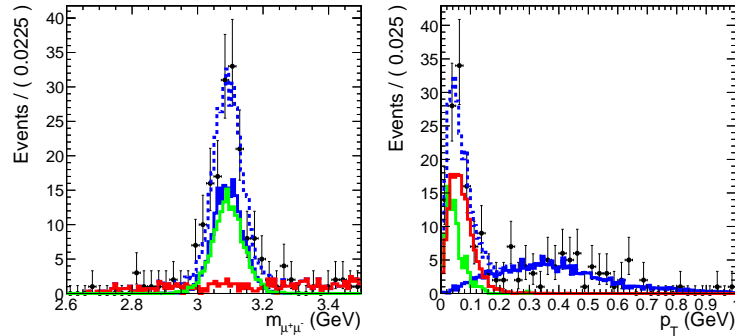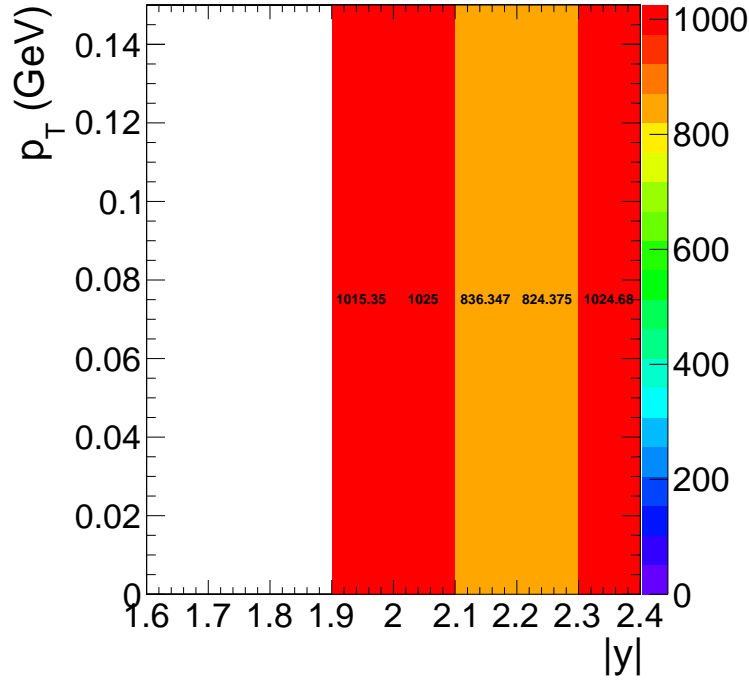


Figure 4.26: Yields corrected by the MC incoherent acceptance map.

The effect of polarization was estimated by correcting by the acceptance for an polarized J/$\psi$ sample.

### 4.7.7 ZDC reconstruction

An additional method for estimating the ZDC neutron thresholds was used to estimate the systematic errors on the threshold measurements. This additional method used in previous ZDC measurements differs in the way the signal time slices are used to calculate the the signal from each channel. In the standard method used in previous analyses, the signal is taken from the sum of time slices 4, 5, and 6. To estimate the event by event noise pedestal the sum of time slice 1 and 2 are used. The signal for an individual ZDC channel is then calculated as the sum of the signal time

Figure 4.27: Yields corrected by an unpolarized J/$\psi$ sample.

slices minus the sum of the noise time slices weighted by a factor of 3/2 to account for the differing number of noise versus signal time slices. In the standard method, the EM section is weighted by a factor of 0.1 as in the m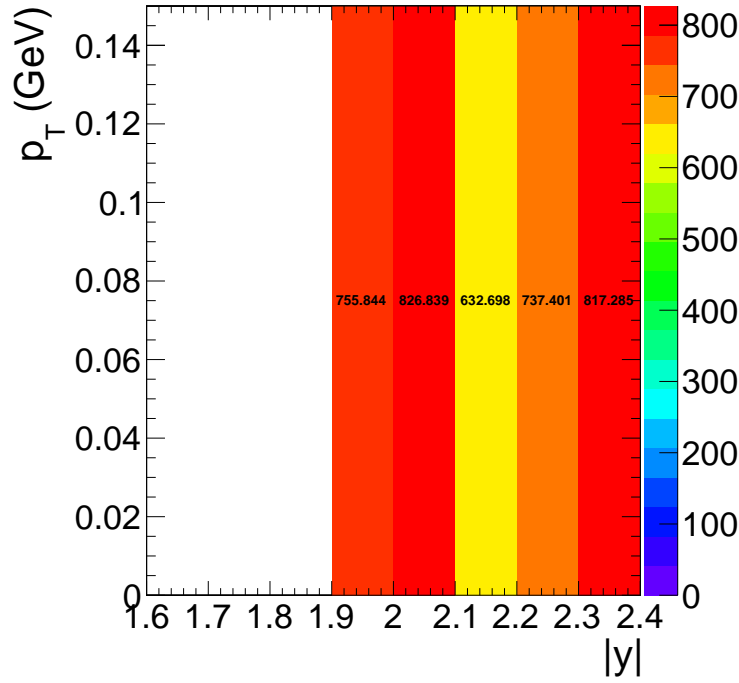ethod described in Section 4.4. The advantage of the standard method is that by using multiple signal and noise time slices the signal and noise are effectively averaged reducing time slice to time slice fluctuations. However, by using time slices 1 and 2 for measuring the noise, the noise can only be measured half the time due to unmeasurable negative fluctuations of the dominant low frequency component of the noise.

The new method relative to the standard method separates low signal from the noise more effectively for each side of the ZDC as whole. This is particularly important for ZDC$^+$ where the 1st HAD section had a lower gain than the other sections. The ZDC$^+$ and ZDC$^-$ signals near the one neutron peak using the standard and new reconstruction methods were plotted for comparison in Fig. 4.28. In Fig. 4.28, the shrinking of width of the noise peak around zero in the new method versus the old method is apparent for both ZDC$^+$ and ZDC$^-$.

Timing cuts were applied to enhance the signal relative to the background in order to resolve
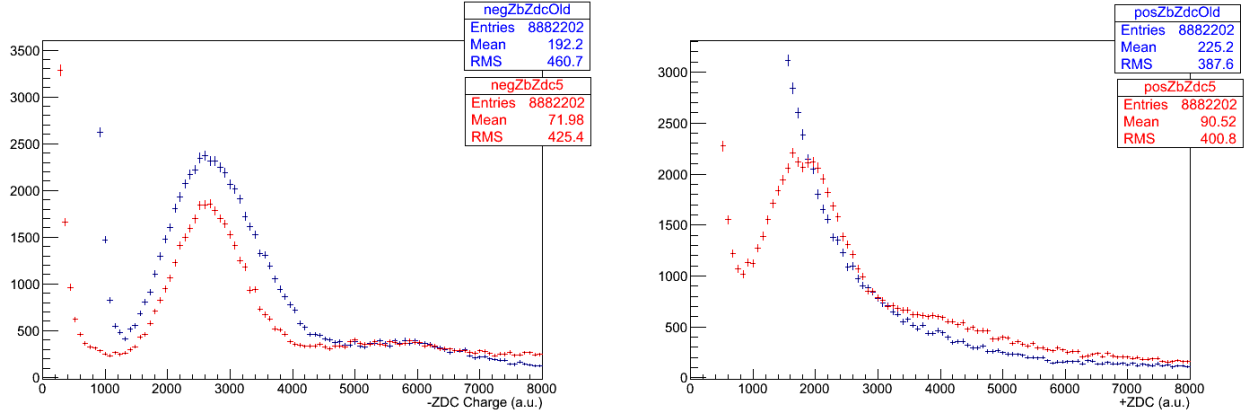
Figure 4.28: Comparison of the new ZDC reconstruction method and the standard method for ZDC$^-$ (left) and ZDC$^+$ (right).

the one neutron peak in ZDC$^+$ using the standard method. Because the products of the collision are synced with time slice 4, noise can be rejected by selecting channels where the maximum signal falls into time slice 4. The noise will have no preferred time slice (see Fig. 4.3). Using this fact, signal can be preferably selected by requiring that the hadronic channels of the ZDC have a peak signal in the fourth time slice. Through these timing cuts the single neutron peak was recovered using the standard reconstruction for ZDC$^+$.

To examine the effectiveness of the timing cuts, event by event noise subtraction was removed from the standard reconstruction. The signal from each channel was taken from time slices 4,5, and 6 with out subtracting 1 and 2. The signal spectrum from ZDC$^-$ was then plotted with the result shown in Fig. 4.29. As each additional hadronic channel is required to have a maximum signal in the fourth time slice, the single neutron peak emerges. Fig. 4.29 demonstrates that the single neutron peak can be recovered from the noise using timing cuts alone.

Using the noise subtraction method described by Method 1, the same signal emerges. Fig. 4.30 confirms that both noise subtraction and the timing require produce the same signal. This gives confidence that the signal is not an artifact of either cut, but the true neutron signal.

The spectrum for method 1 and 2 are fit to a series of Gaussians.

Fig. 4.30 and Fig. 4.28 demonstrate the consistence of the using timing cuts and noise subtraction to enhance the signal neutron peak. Fig. 4.30 confirms the legitimacy of the noise subtraction
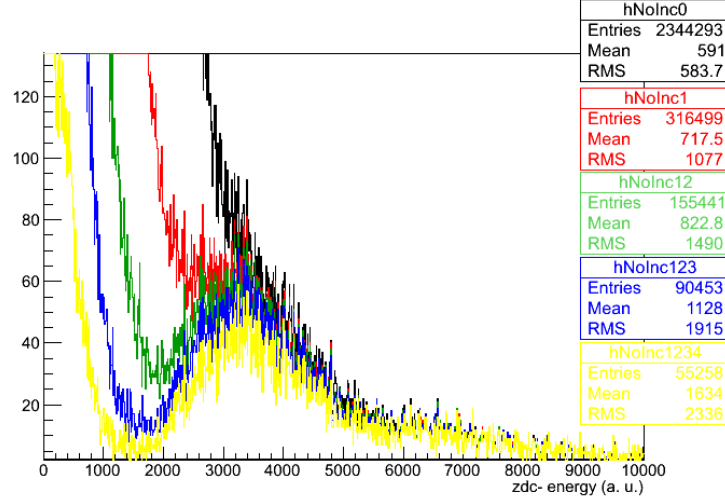
Figure 4.29: Effects of requiring in-time signal in successively more ZDC hadronic channels, no timing, at least one, at least two, at least three, and all four HAD channels have a maximum signal in the fourth time slice.

method in $ZDC^-$ by showing the that the same signal emerges from the noise subtraction method as the timing method. Fig. 4.28 demonstrates the corresponds between between noise subtraction method 1 and method 2 on in $ZDC^-$ where signal is better separated from the electronic noise. This allows for confidence that the signal seen in $ZDC^+$ using method 2 is the one neutron peak.

### 4.7.8   ZDC efficiency

To estimate systematic errors in the ZDC trigger efficiency, the trigger efficiency was measured from five additional samples.

| ZDC Side | Reco Method | $N_{events}$ | $N_{trig}$ | $\varepsilon_{ZDC}$ |
|---|---|---|---|---|
| $(ZDC^+$ or $ZDC^-)$ and 1 pixel track | | | | |
| $ZDC^+$ | 1 | 72946 | 71688 | $0.982 \pm 0.005$ |
| $ZDC^+$ | 2 | 73028 | 71706 | $0.9819 \pm 0.005$ |
| $ZDC^-$ | 1 | 76137 | 71786 | $0.9429 \pm 0.005$ |
| $ZDC^-$ | 2 | 76132 | 71859 | $0.9439 \pm 0.005$ |
| $(ZDC^+$ or $ZDC^-)$ | | | | |
| $ZDC^+$ | 1 | 30986 | 30333 | $0.9789 \pm 0.0079$ |
| $ZDC^+$ | 2 | 31029 | 30339 | $0.9778 \pm 0.0079$ |
| $ZDC^-$ | 1 | 39178 | 30164 | $0.7699 \pm 0.0059$ |
| $ZDC^-$ | 2 | 35703 | 30443 | $0.8527 \pm 0.0067$ |
| Zero Bias | | | | |
| $ZDC^+$ | 1 | 109967 | 101598 | $0.9239 \pm 0.0040$ |
| $ZDC^+$ | 2 | 110230 | 101561 | $0.9214 \pm 0.0040$ |
| $ZDC^-$ | 1 | 253241 | 86660 | $0.3422 \pm 0.0013$ |
| $ZDC^-$ | 2 | 156336 | 87401 | $0.5591 \pm 0.0024$ |
| Zero Bias with ZDC timing cuts | | | | |
| $ZDC^+$ | 1 | 88676 | 84429 | $0.9521 \pm 0.0046$ |
| $ZDC^+$ | 2 | 88480 | 84202 | $0.9517 \pm 0.0046$ |
| $ZDC^-$ | 1 | 59878 | 54728 | $0.9140 \pm 0.0054$ |
| $ZDC^-$ | 2 | 60467 | 54733 | $0.9052 \pm 0.0053$ |
| $(ZDC^+$ or $ZDC^-)$, 1 pixel track, and L1 Muon trigger | | | | |
| $ZDC^+$ | 1 | 65466 | 63376 | $0.9681 \pm 0.0054$ |
| $ZDC^+$ | 2 | 65543 | 63358 | $0.9667 \pm 0.0054$ |
| $ZDC^-$ | 1 | 71929 | 63512 | $0.8830 \pm 0.0048$ |
| $ZDC^-$ | 2 | 72932 | 63582 | $0.8718 \pm 0.0047$ |
| $(ZDC^+$ or $ZDC^-)$, 1 pixel track, and L1 EG trigger | | | | |
| $ZDC^+$ | 1 | 613758 | 602123 | $0.9810 \pm 0.0018$ |
| $ZDC^+$ | 2 | 614014 | 601863 | $0.9802 \pm 0.0018$ |
| $ZDC^-$ | 1 | 643905 | 602671 | $0.9360 \pm 0.0017$ |
| $ZDC^-$ | 2 | 647888 | 603089 | $0.9309 \pm 0.0017$ |

Table 4.10: ZDC trigger efficiencies for ZDC reconstruction method 1 and 2 for different trigger samples

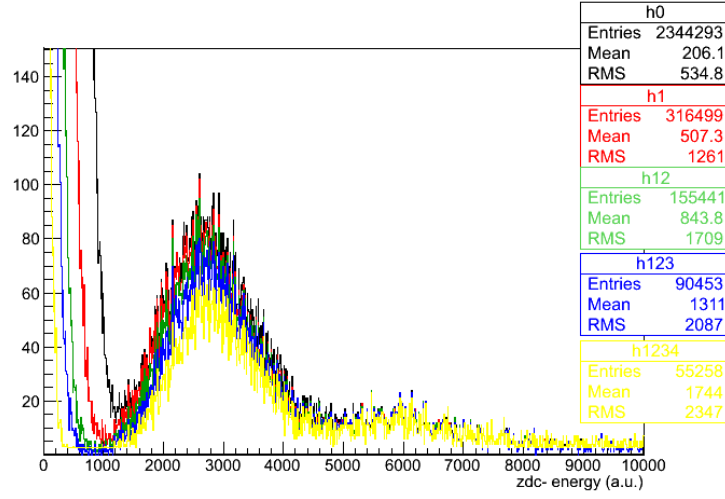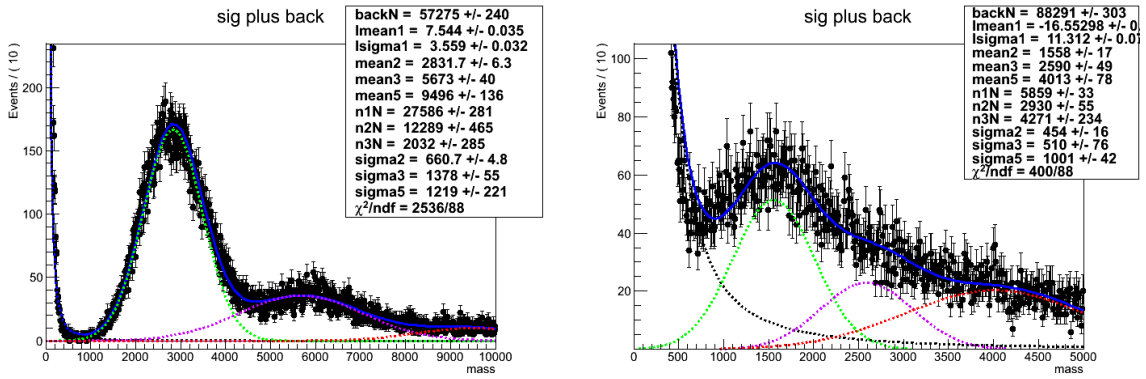Figure 4.30: Effect of ZDC signal timing requirements after noise subtraction.



Figure 4.31: Fit to charge spectrum from $ZDC^-$ (left) and $ZDC^+$ (right) using method 1

71

# Chapter 5

# Results

## 5.1    Coherent cross section

For the coherent cross section, the raw yield of dimuon candidates was measured after applying the cuts described in Section 4.3.
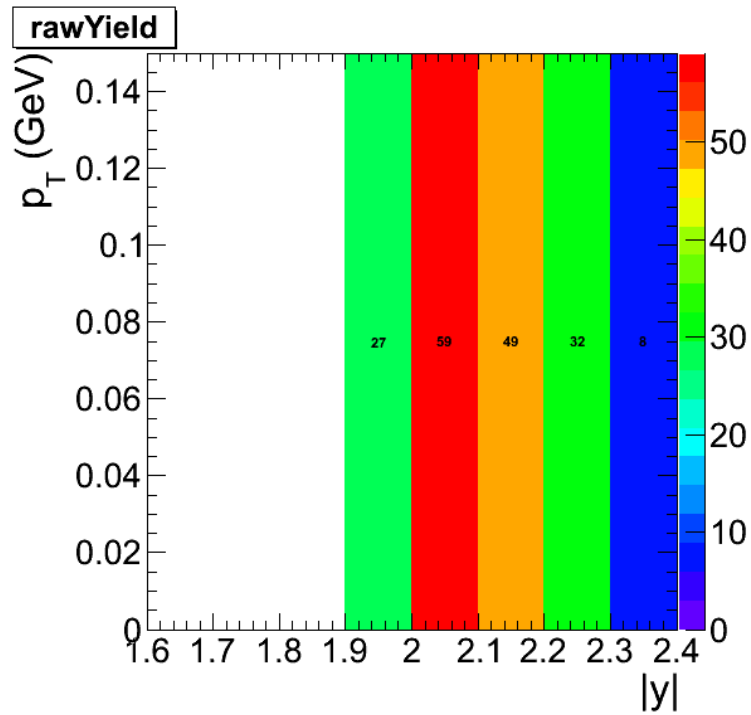


Figure 5.1: Raw yield for the Coherent cross section measurement.

The raw yields were divided by the total efficiency times acceptance factors to produce corrected yields.
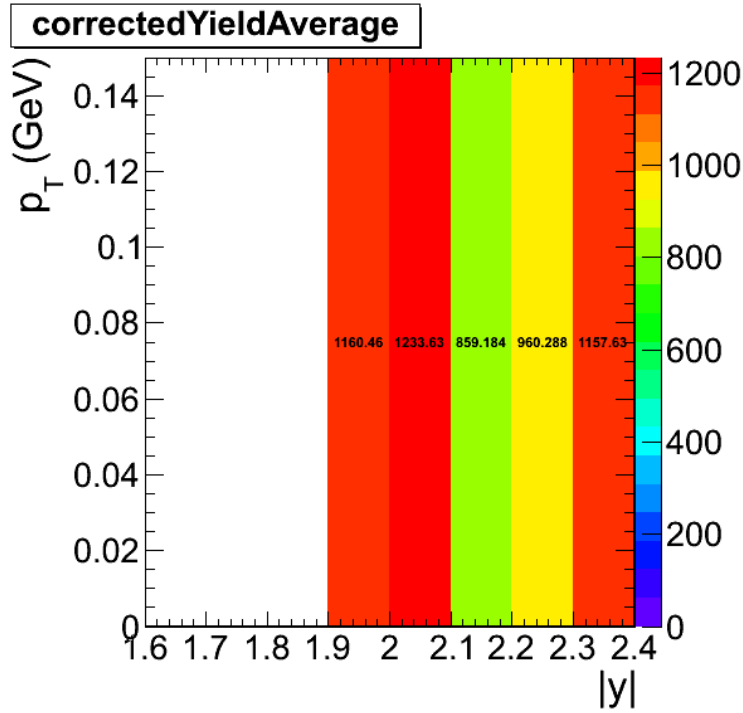


Figure 5.2: Corrected yields for the coherent $p_T$ region.

The corrected yields in the 2.0-2.1 and 2.1-2.2 $|y|$ rapidity bins were added together to calculate the cross section. These bins were selected to insure a total acceptance times efficiency greater than 5%.

The contribution from coherent production was estimated from the template fit in Fig. 4.22. The first three bins are used to estimate the contribution below 150 MeV.

## 5.2 Incoherent cross section

## 5.3 Break up ratios

In Table 5.3 the ratio between raw yields for different break up modes are shown.

Fig. 5.3 and Fig. 5.4 compare the raw break up ratios two STARlight and LTA predictions.
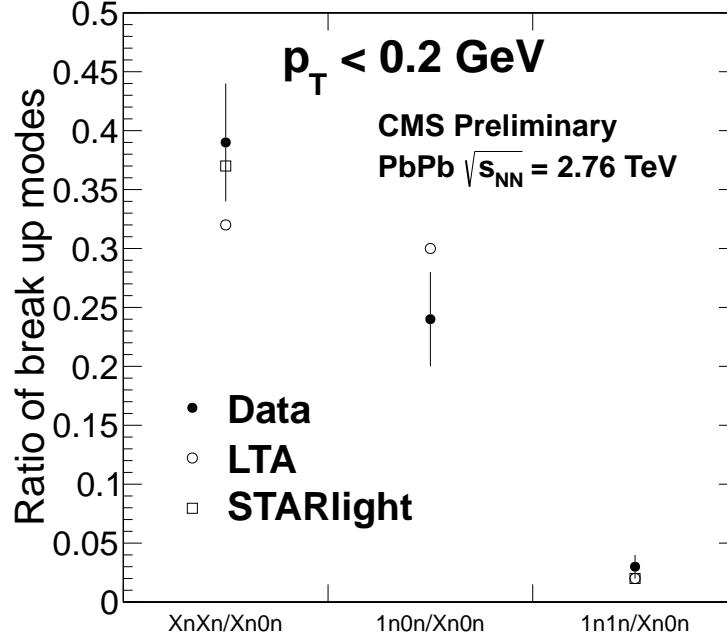
Figure 5.3: Ratio between J/$\psi$ yeilds XnXn and 1n0n break-up modes compared the Xn0n break-up mode for J/$\psi$ with $p_T$ below 150 MeV.

In Table 5.1 the ratio between break up modes are shown for different theories and processes.

Table 5.1: Number of J/$\psi$ integrated over $p_T$ and $y$ with statistical uncertainty.

|  | $X_nX_n/X_n0_n$ | $1_n0_n/X_n0_n$ | $1_n1_n/X_n0_n$ |
|---|---|---|---|
| STARlight coherent | 0.37 | - | 0.02 |
| Zhalov coherent | 0.32 | 0.30 | 0.02 |
| STARlight incoherent | 0.37 | - | 0.007$\pm$0.02 |

## 5.4 diMuon-neutron correlations

The invariant mass distribution for different break-up modes is show for the coherent and incoherent J/$\psi$ on the Fig. 5.5 and Fig. 5.6 respectively.

The number of the coherent and incoherent J/$\psi$ for each break-up mode are given in the Tab. 5.2. The ratios between the modes $X_nX_n$, $1_n0_n$, $1_n1_n$ and the mode $X_n0_n$ are given in the table Tab. 5.3. Some of the ratios can be obtained from STARLIGHT and from the Zhalov and thus
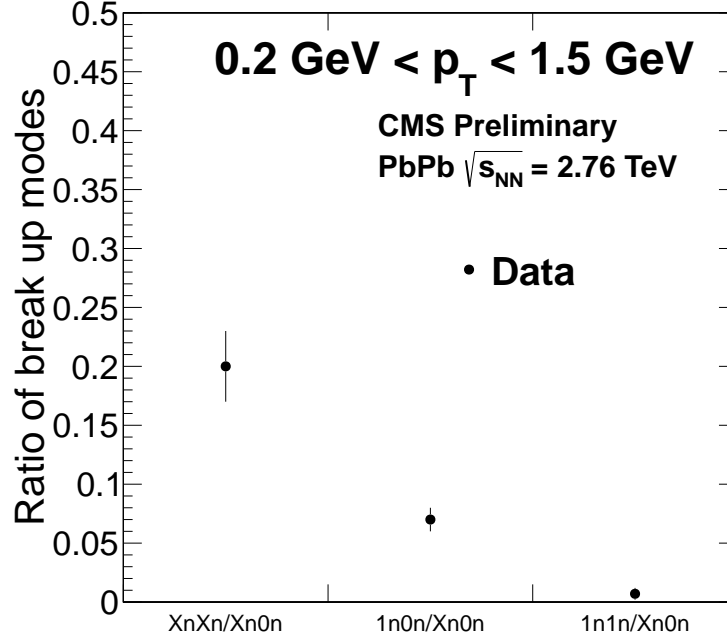
Figure 5.4: Ratio between J/$\psi$ yeilds XnXn and 1n0n break-up modes compared the Xn0n break-up mode for J/$\psi$ with $0.2 < p_T < 1.5$ GeV.



Figure 5.5: Invariant mass spectrum of the opposite signs di-muons originating from the coherent J/$\psi$ for $X_n0_n$ breakup mode for two invariant mass regions.

are given in Tab. 5.1.

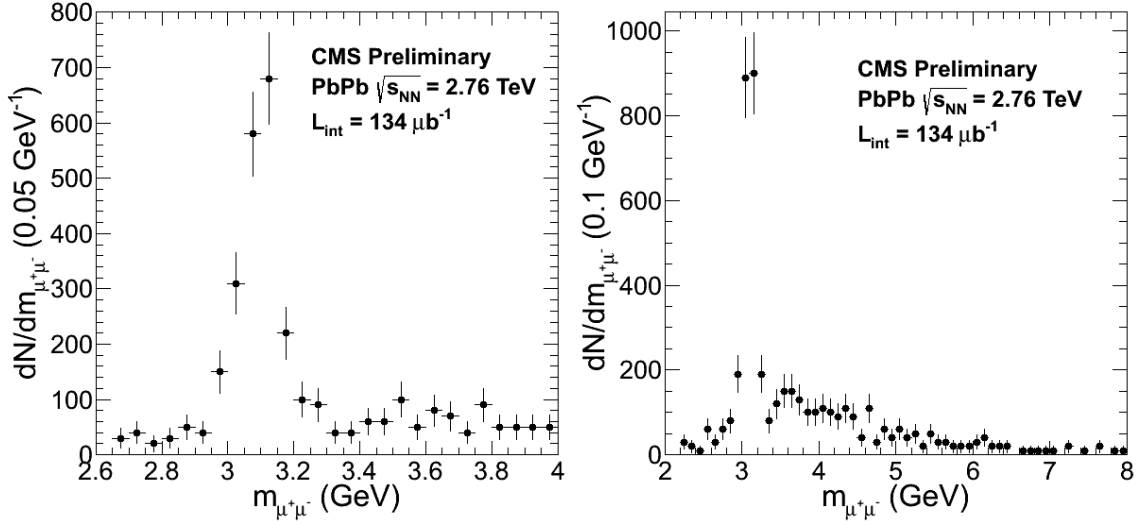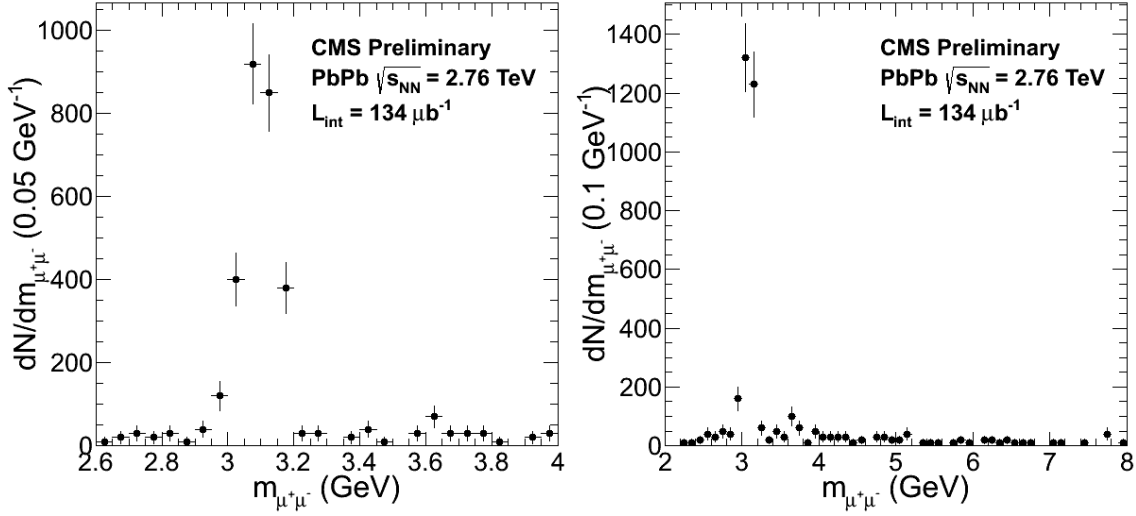For statistical reason, further studies concentrate only on the break-up mode $X_n0_n$.

Figure 5.6: Invariant mass spectrum of the opposite signs di-muons originating from the incoherent J/$\psi$ for $X_n0_n$ breakup mode for two invariant mass regions.

Table 5.2: Number of coherent J/$\psi$ integrated over $p_T$ and $y$ with statistical uncertainty.

|  | $X_n0_n$ | $X_nX_n$ | $1_n0_n$ | $1_n1_n$ |
|---|---|---|---|---|
| coherent J/$\psi$ | 242±16 | 94±10 | 58±8 | 8±3 |
| incoherent J/$\psi$ | 291±17 | 57±8 | 19±4 | 2±1 |

Figure 5.7 shows the transverse momentum distribution of the J/$\psi$ (coherent and incoherent) in the case when J/$\psi$ and neutron have the same or opposite rapidity direction. The ratio between the J/$\psi$ and neutron that have the opposite direction and the J/$\psi$ and neutron that have the same direction i shown on Fig. 5.8. The red curve gives the pure theory calculations, the black one gives the theory results that are injected to the detector simulation and thus taking into account experimental bias.

The rapidity distributions of the coherent and incoherent J/$\psi$ are shown in the Fig. 5.9. They are shown separately for the events firing the ZDC$^+$ and ZDC$^-$. The same distributions are also obtained for the MC and shown in Fig. 5.10. For the MC the particle gun generator with the input $p_T$ spectrum from Zhalov's calculation (LTA). The rapidity symmetry for coherent J/$\psi$ and asymmetry for incoherent J/$\psi$ are observed in data and MC. These are quantified in the Tab. 5.4.

Table 5.4 gives the number of coherent and incoherent J/$\psi$ separately for the events that fired the ZDC$^-$ and ZDC$^+$. We quote separately the J/$\psi$ that have the same or opposite rapidity direc-

Table 5.3: Number of coherent J/$\psi$ integrated over $p_T$ and $y$ with statistical uncertainty.

|  | $X_nX_n/X_n0_n$ | $1_n0_n/X_n0_n$ | $1_n1_n/X_n0_n$ |
|---|---|---|---|
| coherent J/$\psi$ | 0.39±0.05 | 0.24±0.04 | 0.03±0.01 |
| incoherent J/$\psi$ | 0.20±0.03 | 0.07±0.02 | 0.007±0.005 |
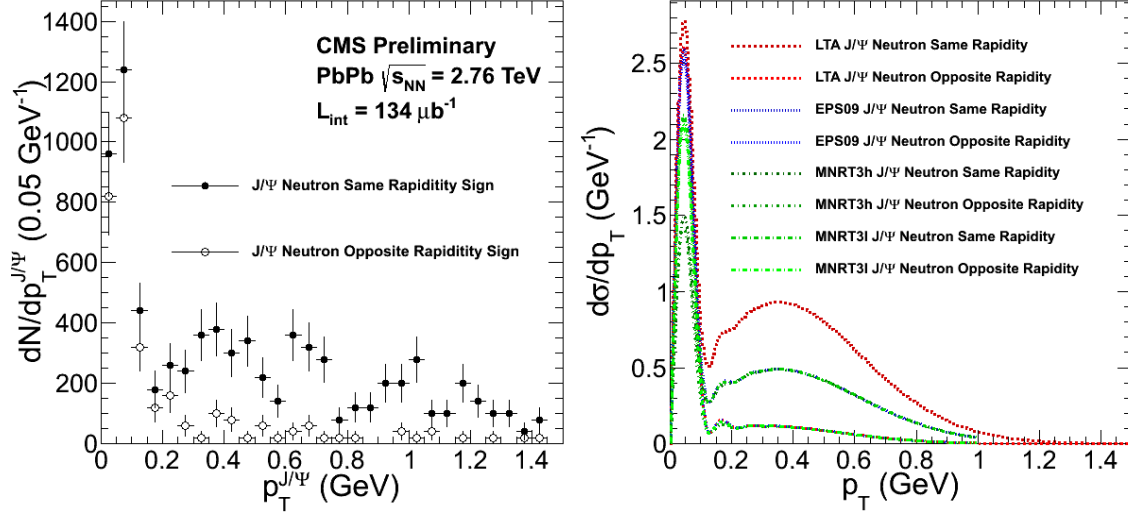


Figure 5.7: Transverse momentum distribution of the J/$\psi$ when J/$\psi$ and neutron have the same or opposite rapidity direction from data (left) and from theory (right).

tion to the neutron direction. The ratios, as described below are also given in the Tab. 5.4: $R_{ZDC-}^{y^+/y^-}$ : ratio between the number of J/$\psi$ having $y > 0$ to the number of J/$\psi$ having $y < 0$ from the events that fired ZDC$^-$

$R_{ZDC+}^{y^-/y^+}$ : ratio between the number of J/$\psi$ having $y < 0$ to the number of J/$\psi$ having $y > 0$ from the events that fired ZDC$^+$

Table 5.4: Final number of J/$\psi$ (for both ZDCs and for two negative and positive rapidity) and ratios with statistical uncertainty.

|  | ZDC$^-$ $y<0$ | ZDC$^-$ $y>0$ | $R_{ZDC-}^{y^+/y^-}$ | ZDC$^+$ $y<0$ | ZDC$^+$ $y>0$ | $R_{ZDC+}^{y^-/y^+}$ |
|---|---|---|---|---|---|---|
| coherent J/$\psi$ | 63 | 68 | 1.08±0.19 | 42 | 69 | 0.61±0.12 |
| incoherent J/$\psi$ | 141 | 26 | 0.184±0.039 | 13 | 111 | 0.117±0.034 |

The combined ratio $R_{opp/same}^c$ is calculated as

77
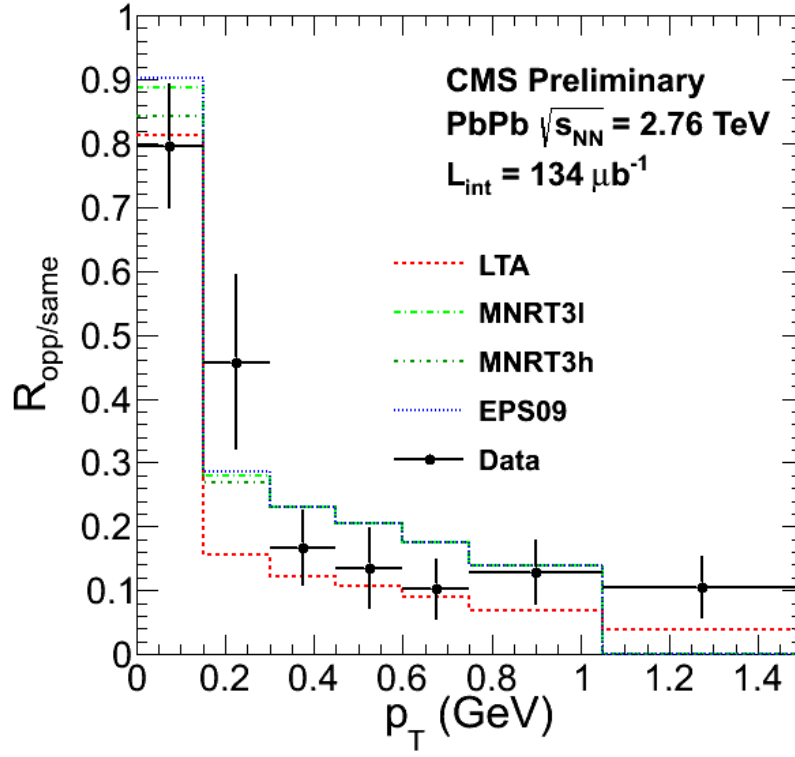
Figure 5.8: Ratio between the transverse momentum distribution of the J/$\psi$ when J/$\psi$ and neutron have the opposite direction and the transverse momentum distribution of the J/$\psi$ when J/$\psi$ and neutron have the same direction.

$$R^c_{opp/same} = \frac{ZDC^- \text{and } y > 0 + ZDC^+ \text{and } y < 0}{ZDC^- \text{and } y < 0 + ZDC^+ \text{and } y > 0}$$

- $R^c_{opp/same}$ for coherent J/$\psi$= $0.83 \pm 0.12$.

- $R^c_{opp/same}$ for incoherent J/$\psi$= $0.155 \pm 0.021$.

The correction factors (efficiency, reconstruction) are as following:

- $\varepsilon_{ZDC^-}$: efficiency of the ZDC$^-$ of 0.98

- $\varepsilon_{ZDC^+}$: efficiency of the ZDC$^+$ of 0.94

- $\varepsilon_{\mu^-}$: efficiency × reconstruction of the muons with rapidly <0: 1.0

- $\varepsilon_{\mu^+}$: efficiency × reconstruction of the muons with rapidly >0: 1.014.

The combined ratio $R^{ceff}_{opp/same}$ corrected with the factors above is calculated as

$$R^{ceff}_{opp/same} = \frac{\varepsilon_{ZDC^-}\varepsilon_{\mu^+}ZDC^- \text{and } y > 0 + \varepsilon_{ZDC^+}\varepsilon_{\mu^-}ZDC^+ \text{and } y < 0}{\varepsilon_{ZDC^-}\varepsilon_{\mu^-}ZDC^- \text{and } y < 0 + \varepsilon_{ZDC^+}\varepsilon_{\mu^+}ZDC^+ \text{and } y > 0}$$

$R^{ceff}_{opp/same}$ is 0.83± 0.12.

- $R^{ceff}_{opp/same}$ for coherent J/$\psi$= 0.83 ± 0.12.

- $R^{ceff}_{opp/same}$ for incoherent J/$\psi$= 0.154 ± 0.021.

If considering 3 significant figures for the representation of the result these values are:

- $R^{c}_{opp/same}$ for coherent J/$\psi$= 0.833 ± 0.124

- $R^{c}_{opp/same}$ for incoherent J/$\psi$= 0.155 ± 0.021

- $R^{ceff}_{opp/same}$ for coherent J/$\psi$= 0.828 ± 0.124

- $R^{ceff}_{opp/same}$ for incoherent J/$\psi$= 0.154 ± 0.021

This shows that in this measurement the efficiencies factors are negligible.
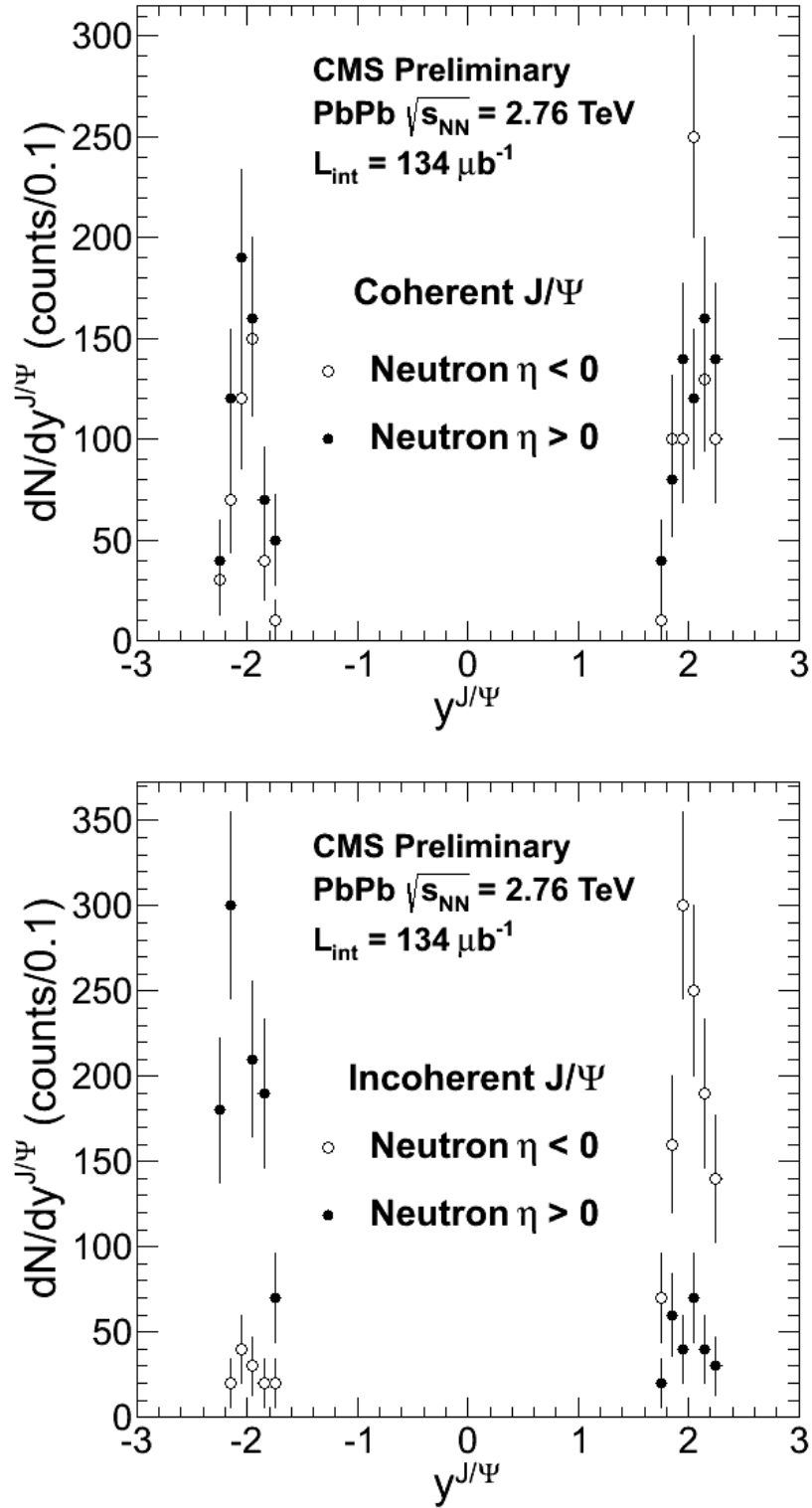
Figure 5.9: The rapidity distribution of the coherent (top) and incoherent (bottom) J/$\psi$ for the ZDC$^+$ and ZDC$^-$.
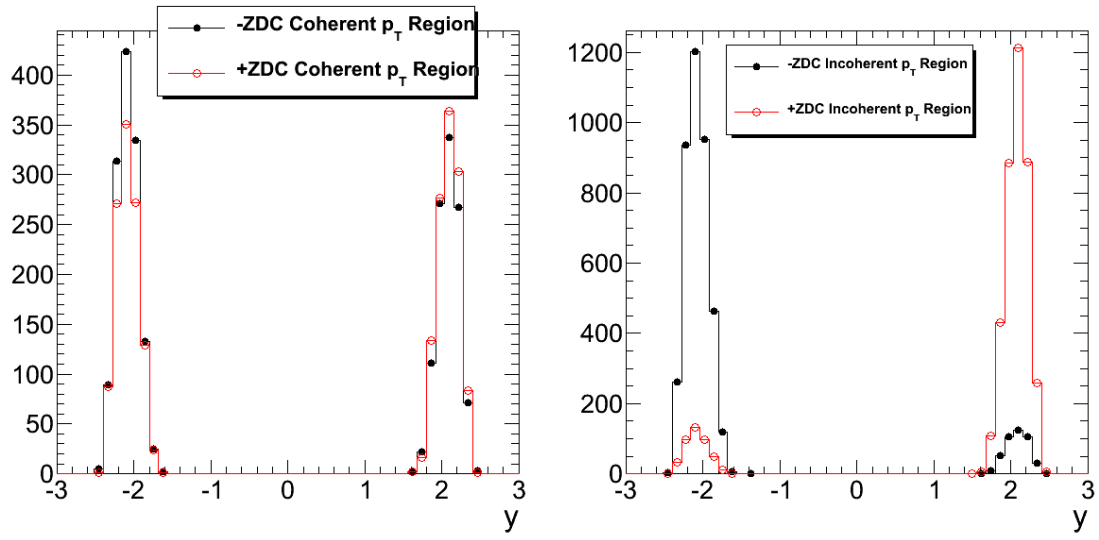
Figure 5.10: The rapidity distribution of the coherent (left) and incoherent (right) J/ψ for the ZDC$^+$ and ZDC$^-$ from MC (particle gun with customized $J/\psi p_T$ input distribution).

# Chapter 6

# Conclusion

## 6.1   xsection results

## 6.2   correlation results

# Chapter 7

# Future Works

## 7.1 Studies of 2011 PbPb data

### 7.1.1 High mass $\gamma - \gamma \rightarrow e^+ e^-$ in PbPb 2011

A study of the di-electron production in UPC events is already possible from the recorded 2011 data. This measurement would make use of the electron triggers and combined the current di-muon data with di-electron data from the triggers using the ECAL. The electron triggered sample potentially offers a large increase in statistics. By adding the additional channel the statistics would already increase. However in addition to this, because of the smaller mass of the electron, di-electron production is slightly favor compared to di-muon production. STARlight predicts that di-electron cross section is a factor of more than 2.5 higher in Xn break-up mode than the di-muons channel when looking at masses above 4 GeV. The acceptance for electrons in potential higher as well. The ECAL is position just beyond the tracker, whereas the muon system is outermost sub-detector. This elevates the main reduction of muon acceptance, which is the material budget. There is simply a lot a detector in front the muon system.

In order to perform the study several key additions would need to be made relative to the current di-muon analysis. The original reconstruction of the data used in the current di-muon analysis does not contain electron objects. Either the analysis would have to migrated to reconstruction of the

data done in a newer software version, or reconstruction of the electrons would have to be added to the current analysis chain. There are currently no electron UPC MC samples produced. In order to study the acceptance and efficiency for electrons these samples would be need. The ultimate limitation on this study is the 2 GeV threshold in $p_T$ in the ECAL trigger. This limits the di-electron mass range to where the trigger is efficient.

The contribution of higher order diagrams can be explored by the photoproduction of di-lepton pairs is to explore. With additional contributions to the physics communities understanding of this process this study will help to determine necessity or non-necessity of including higher order of corrections in simulations such as STARlight. Having an additional channel to help constrain the current di-muon measure of the of UPC $\gamma - \gamma$ interaction will also help to constrain the $J/\psi$ measurement by adding a data driven check on the normalization $\gamma - \gamma$ background to the $J/\psi$


## 7.1.2   UPC Hadronic Overlap and PbPb 2011

In the model calculations explored in this analysis of UPC quarkonia photoproduction all hadronic interactions are rejected. Photoproduction in events where hadronic interactions occur are not included in the cross section calculation. However, inclusive $p_T$ spectra of $J/\psi$ measured by ALICE in peripheral PbPb collisions show a low momentum peak consistent with coherent photoproduction [15]. CMS has the opportunity to explore this overlap between hadronic interactions and photoproduction using PbPb data from 2011 that is already recorded.

To study the overlap between photoproduction and hadronic proctuction of quarkonia event the inelastic sample and the UPC sample could both be used. The looseness of the veto designed to reject hadronic interactions, which uses the BSC detector, leaves a significant overlap with peripheral hadronic collisions. The inclusive quarkonia sample from typical hadronic collisions can also be utilized. Coherent quarkonia photoproduction has a distinctive low $p_T$ structure that can be used to identify photoproduced candidates in a sample that contains photoproduction combined with hadronic interactions. This measurement would open up the door to exploring the boundary between photoproduction and hadronic production. By looking at the mixing of the two, both
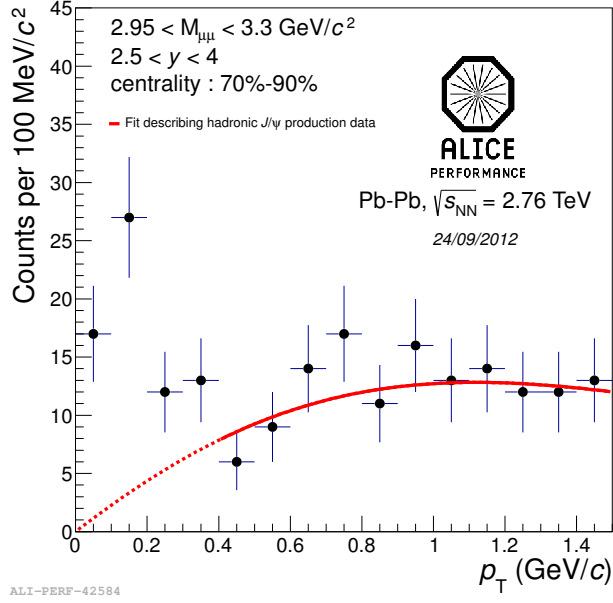
Figure 7.1: Coherent excess in inclusive $J/\psi$ $p_T$ spectrum.

process, hadronic production and photoproduction, will be better understood.

In order to compliment each others strengths, the inclusive hadronic sample and the UPC sample of dimuon candidates would be utilized in this study. The two samples muon and centrality biases are orthogonal allowing each to serve as a check on the other. The inclusive hadronic sample is triggered by a higher $p_T$ threshold double trigger, whereas the UPC sample is uses a lower $p_T$ single muon trigger. The UPC sample is strongly biased toward peripheral events, which would lead to inefficiencies as events become more central, whereas, the inclusive sample is slightly biases in the most peripheral events due to an inefficiency an event selection efficiency in the most peripheral centrality bin. If these offsetting biases can be exploited, clarity about the transition between and mixing of photoproduction and hadronic production of quarkonia can be produced. A measurement of the kind proposed here will both produce a better understanding of the low $p_T$ portion of the inclusive spectrum as well as the hadronic overlap with UPC measurements.

### 7.1.3 UPC with muons in HF

As higher rapidities are explored both lower and higher momentum partons of the nucleus are probed. Because these two contributions to the UPC photoproduction cross section can be separated using neutron tagging in incoherent events, exploring higher dimuon rapidities becomes attractive. HF extends to 5 in $\eta$, 2.6 units beyond the edge of the tracker. By combining hits in HF with tracks in the tracker the higher dimuon rapidities could be explored. When combined with neutron tagging of incoherently produced quarkonia, the current study can be extended to probe lower-x nuclear partons by identifying muons in HF.

## 7.2 Studies of 2013 pPb data and 2015 PbPb data

Specific UPC triggers were also developed for the pPb run in 2013. For this period of running a much higher total trigger rate was read out relative to 2011. The total rate allocated for UPC triggers at the L1 in 2013 was 5kHz and 50 Hz at the HLT. This factor of 5 increase in the bandwidth, especial in L1 rate, allowed for a different triggering strategy than in 2011.

The basic strategy in 2013 was the same as in 2012, use the loosest available ECAL and muon L1 triggers to push to capture the lowest $p_T$ electrons and muons possible and veto on hadronic interactions, but was impemented differently. Because of the L1 bandwidth restrictions in 2011, both the ZDC and the BCS were used on the L1 to reduce rates. In 2013 only the muon and ECAL triggers were used on the L1 allowing for rejection of hadronic interactions through cuts on track multiplicity. In addition, a more sophisticated trigger using full dimuon reconstructed was developed to increase purity. The main advantage in this shift in strategy was a higher purity due to the increased sophistication of the reconstruction on the HLT. In addition, an increase in cross section of the underlying physics process was achieved by relaxing the neutron emission requirement.

The HLT triggers in 2013 rejected hadronic interactions through counting tracks. For the five UPC trigger paths included in the HLT meanu, three levels of reconstruction were done at the HLT.

Pixel tracks were reconstructed from the inner pixel section of the silicone tracker alone, tracks were reconstructed using the full tracker using the strips as well, and full dimuon reconstruction was done using the tracker and muon detector. The least restrictive pixel track paths required at least one track reconstructed from the pixel detector and less than 10 pixel tracks in the event. Full tracking paths were added on top of the pixel track paths and included an additional requirement of one full track and less than 7 reconstructed tracks. The most restrictive path added to the pixel and full tracking paths and required reconstruction of dimuons with a mass between 2 and 10 GeV. The design of these triggers allowed for higher signal purity relative to 2012 through use of full tracking on the HLT and allowed for increased exposure to the cross section by removing the break-up requirement implicit in requiring a ZDC trigger on the L1.

The PbPb run in 2015 will be at higher beam energies and luminosities. The $sqrts_{NN}$ will increase from 2.76 TeV in 2011 to 5.1 TeV with a project integrated luminosity between $0.3/nb$ and $1/nb$. The factor of 2 to 10 increase in integrated luminosity will increases the number of events directly. In addition, both the increase in energy, which increases the photon flux, and the ability to utilize the 2013 trigger strategy of sifting the onus of the trigger selection to the HLT will increase the measured yields relative to 2011. The higher beam energy, higher integrated luminosity, and added selectivity of the HLT will create the opportunity to explore both $J/\psi$ with greater statistical precision and novel objects such as $\Upsilon$, and jets.

### 7.2.1   pPb $J/\psi$

$J/\psi$ photoproduciton in pPb collisions is dominated $\gamma - p$ interactions. The measurement would primarily probe the proton gluon densities. In Eq. 2.13 the photon flux depends on the square of the number of protons in parent nucleus, $Z^2$. However, the cross section of the target only increase as the total number of nucleons to the 2/3rds power, $A^{2/3}$. The much higher photon flux from the Pb ion more than compensates for the decreased size of the proton.

A pPb UPC $J/\psi$ measurement will compliment the measurements done at HERA, and measurements done by ALICE. CMS will contribute by adding additional kinematic coverage and

cover a unique range of proton-photon center of mass energies, $W_{p\gamma}$. The difference in beam energies and species at LHC versus HERA result in access to different $W_{p\gamma}$. ALICE and CMS have different acceptance in $J/\psi$ rapidity, which also translates to coverage of different $W_{p\gamma}$. In addition, an excess in the UPC cross section compared to HERA measurements would indicate a non-exclusive contribution to the pPb UPC $J/\psi$ cross section. This measurement will both help enhance the current understanding of the $p\gamma$ $J/\psi$ photoproduction cross section as a function of $W_{p\gamma}$, and validate the UPCs measurements as an extension of the work done at HERA.

### 7.2.2   UPC $J/\psi$ and $\Upsilon$ in 2015

A measurement of the UPC $J/\psi$ in 2015 will produce a strong constraint on the low-x portion of the nuclear gluon distribution relative to the current analysis form the 2011 data. The $J/\psi$ measurement will probe lower-x than in 2011 due to the increase in beam energy. A measurement in 2015 will also have lower statistical errors due to the increase in integrated luminosity and increased L1 bandwidth. UPC $J/\psi$s in 2015 will push farther towards the onset of low-x parton saturation.

Measurement of the UPC $\Upsilon$ cross section from the 2015 data will be the first from PbPb collisions. As with the $J/\psi$, Additional L1 bandwidth, increased beam energy, and and intensity will increase the $\Upsilon$ yield significantly relative to 2011. The acceptance for $\Upsilon$ is near 40% for all rapidities between -2.4 to 2.4 (see Fig 7.2). Conversely, $J/\psi$ acceptance is 8% near 2 in dimuon rapidity only. Below 1.6 in rapidity there is not acceptance for for UPC $J/\psi$. Estimates from STARlight predict a factor of 17-60 increase in yield depending on the total delivered integrated luminosity. The $\Upsilon$ measurement will be a new measurement that will expand the range of x and $Q^2$ probed with a higher energy probe that is better suited to the acceptance of CMS.

### 7.2.3   UPC jets

Like $\Upsilon$s, UPC photoproduction of jets is a novel probe. The LHC 2015 heavy ion run presents an opportunity do this measurement for the first time. The cross section for photoproduction of
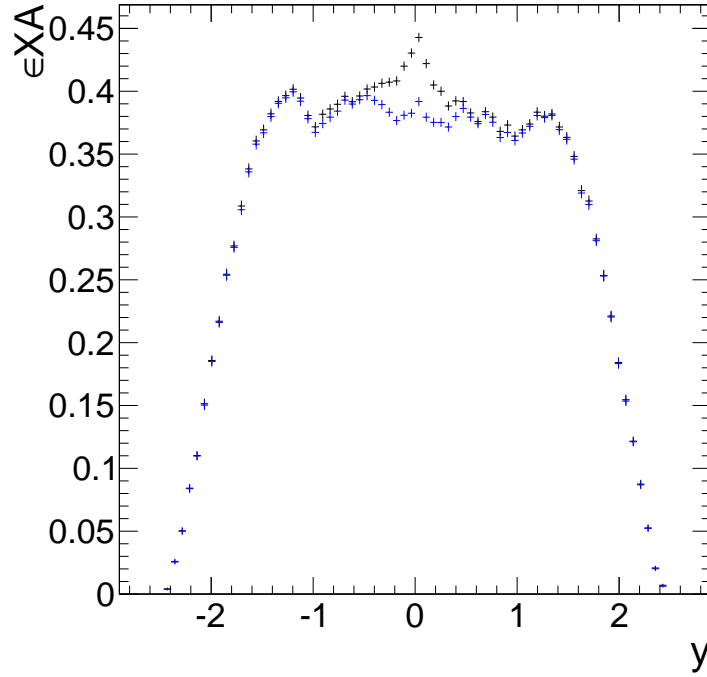
Figure 7.2: $\upsilon$ efficiency times acceptance in CMS from STARlight for $\sqrt{s_{NN}} = 5.1$ TeV as function of $y$.

jets was estimated in Ref [**?**] and found $b\bar{b}$ and $c\bar{c}$ on the order of 1 mb and 1b respectively. With the integrated luminosity expected for 2015 as many as $1x10^6$ $b\bar{b}$ events and $1x10^9$ $c\bar{c}$ events. Jet photoproduction is not constrained by the mass of the bound onia states like in $J/\psi$ and $\Upsilon$ photoproduction. For this reason, jet photoproduction probes a wider range of x and $Q^2$. UPC jets therefore will both expand on the $J/\psi$ and $\Upsilon$ measurements in addition to providing an additional validating compliment to the onia measurements.

The jet measurement will require additional trigger development and analysis design. The jet signal differs significantly from the dimuon signals used in the current analysis. The trigger scheme used in the 2013 pPb run selected UPC events by vetoing events with high numbers of track. The track multiplicity of the jets will not pass this requirement. However, new L1 trigger logic is currently being developed to separate the jet from the underlaying event in nuclear collisions. This trigger logic could also be utilized to select jet events that produce very little to no underlaying event. In addition to the trigger, jet reconstruction algorithms would needed to be adapted to push
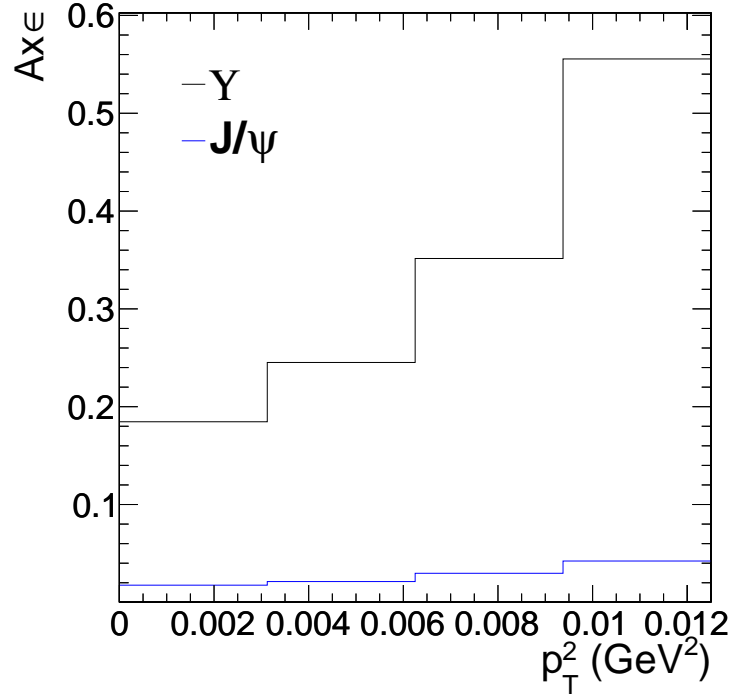
Figure 7.3: Comparison of $\upsilon$ and J/$\psi$ efficiency times acceptance in CMS from STARlight for $\sqrt{s_{NN}} = 5.1$ TeV as function of p$_T$.

to the lower pT jets they are produced by photoproduction. The UPC jet measurement will demand extra preparation compared to the onia measurements, but the development will overlap with many of the goals that are already being pursued by the CMS Heavy Ion group and will allow for wider collaboration.

# References

[1] L. McLerran, "The Color Glass Condensate and Glasma," `arXiv:0804.1736 [hep-ph]`.

[2] S. Chatrchyan *et al.*, "The cms experiment at the cern lhc," *Journal of Instrumentation* **3** no. 08, (2008) S08004. `http://stacks.iop.org/1748-0221/3/i=08/a=S08004`.

[3] **PHENIX Collaboration** Collaboration, A. Adare *et al.*, "Cold Nuclear Matter Effects on $J/\psi$ Yields as a Function of Rapidity and Nuclear Geometry in Deuteron-Gold Collisions at $\sqrt{s_{NN}} = 200$ GeV," *Phys.Rev.Lett.* **107** (2011) 142301, `arXiv:1010.1246 [nucl-ex]`.

[4] F. Gelis, "Color glass condensate and glasma," *Nuclear Physics A* **854** no. 1, (2011) 10 – 17. `http://www.sciencedirect.com/science/article/pii/S0375947410006615`. Saturation, the Color Glass Condensate and the Glasma: What Have We Learned from RHIC?

[5] J. D. Jackson, *Classical electrodynamics*. Wiley, New York, NY, 3rd ed. ed., 1999. `http://cdsweb.cern.ch/record/490457`.

[6] E. Fermi, "On the Theory of Collisions between Atoms and Electrically Charged Particles," in *Electromagnetic Probes of Fundamental Physics*, W. Marciano and S. White, eds., pp. 243–252. Sept., 2003. `hep-th/0205086`.

[7] C. A. Brau, *Modern Problems in Classical Electrodynamics*. Oxford, New York, NY, 1st ed. ed., 2004.

[8] S. R. Klein and J. Nystrand, "Exclusive vector meson production in relativistic heavy ion collisions," *Phys. Rev. C* **60** (Jun, 1999) 014903. http://link.aps.org/doi/10.1103/PhysRevC.60.014903.

[9] V. Rebyakova, M. Strikman, and M. Zhalov, "Coherent rho and J/psi photoproduction in ultraperipheral processes with electromagnetic dissociation of heavy ions at RHIC and LHC," *Phys.Lett.* **B710** (2012) 647–653, arXiv:1109.0737 [hep-ph].

[10] V. Rebyakova, M. Strikman, and M. Zhalov, "Coherent $\rho$ and J/$\Psi$ photoproduction in ultraperipheral processes with electromagnetic dissociation of heavy ions at RHIC and LHC," *Physics Letters B* **710** no. 4–5, (2012) 647 – 653. http://www.sciencedirect.com/science/article/pii/S0370269312003152.

[11] A. Adeluyi and C. A. Bertulani, "Gluon distributions in nuclei probed at energies available at the CERN large hadron collider," *Phys. Rev. C* **84** (Aug, 2011) 024916. http://link.aps.org/doi/10.1103/PhysRevC.84.024916.

[12] A. Adeluyi and T. Nguyen, "Coherent photoproduction of $\psi$ and $\Upsilon$ mesons in ultraperipheral pPb and PbPb collisions at the CERN Large Hadron Collider at $\sqrt{S_{NN}} = 5$ TeV and $\sqrt{S_{NN}} = 2.76$ TeV," *Phys. Rev. C* **87** (Feb, 2013) 027901, arXiv:1302.4288 [nucl-th]. http://link.aps.org/doi/10.1103/PhysRevC.87.027901.

[13] **ALICE** Collaboration, B. Abelev *et al.*, "Coherent $J/\psi$ photoproduction in ultra-peripheral Pb-Pb collisions at $\sqrt{s_{NN}} = 2.76$ TeV," *Physics Letters B* **718** no. 4–5, (2013) 1273 – 1283. http://www.sciencedirect.com/science/article/pii/S0370269312012257.

[14] V. Guzey, E. Kryshen, M. Strikman, and M. Zhalov, "Evidence for nuclear gluon shadowing from the ALICE measurements of pbpb ultraperipheral exclusive production," *Physics Letters B* **726** no. 1–3, (2013) 290 – 295. http://www.sciencedirect.com/science/article/pii/S0370269313006825.

[15] A. Lardeux, "J/$\psi$ production in Pb-Pb collisions at $\sqrt{s_{NN}}$ =2.76 TeV in the ALICE experiment," *J.Phys.Conf.Ser.* **446** (2013) 012042.

# Appendix A

# My Appendix, Next to my Spleen

There could be lots of stuff here